





# Title

## Optional subtitle

by

### J. Random Author

to obtain the degree of Master of Science  
at the Delft University of Technology,  
to be defended publicly on Tuesday January 1, 2013 at 10:00 AM.

Student number: 1234567  
Project duration: March 1, 2012 – January 1, 2013  
Thesis committee: Prof. dr. ir. J. Doe, TU Delft, supervisor  
Dr. E. L. Brown, TU Delft  
Ir. A. Aaronson, Acme Corporation

*This thesis is confidential and cannot be made public until December 31, 2013.*



An electronic version of this thesis is available at <http://repository.tudelft.nl/>.



# Preface

Preface...

*J. Random Author  
Delft, January 2013*



# Contents



# 1

## Introduction

66 Million years ago, an asteroid the size of Rotterdam initiated what is perhaps the most well known cataclysmic event in the history of life on Earth. With an impact releasing the energy of a billion nuclear bombs, the asteroid left a 180 km crater in the Gulf of Mexico. Launching enough debris into the atmosphere to block out the light of the Sun, eventually leading to the extinction of three quarters of species on Earth, most famously the non-avian dinosaurs (**DinosaurAsteroid**). In recorded human history, a multitude of noteworthy asteroids have impacted Earth, such as the Tunguska impactor in 1908 in Siberia. Flattening over 2000 km<sup>2</sup> of forest, events such as this serve as a staunch reminder of the massive kinetic energy that can be released by an object descending to Earth from space, and the danger this poses to human civilization.

Cognizant of such hazard, the United States launched the Spaceguard Survey in 1992, aiming to “identify 90% of near-Earth Asteroids (NEA’s) larger than 1 km within 10 years.” (**Spaceguard**). With improvements in observation technology, more meteors were witnessed and recorded, leading to greater awareness into the frequency and unpredictability of such events. Of course, impacts from space are not a problem exclusive to Earth; as the 1994 impact of comet Shoemaker-Levy 9 into Jupiter proved. This impact showed that impacts of objects large enough to cause global catastrophe were not as highly improbable as once considered, and asteroid identification efforts took off with it.

The initial spaceguard survey goal was completed successfully, and it is known that there are - within reasonable probability - no civilization-ending asteroids destined for Earth impact in the coming millenium. Nevertheless, smaller asteroids can still pose a local threat to human life or property. In addition, much is still unknown about the exact population of near-Earth asteroids, and such knowledge might provide valuable insights into the origin and evolution of the Solar system. Therefore, NASA extended the spaceguard mandate to detect 90% of all NEA’s larger than 140m (**SpaceguardHistory**).

Since then, a lot of progress has been made in cataloguing and identifying smaller NEA’s. Additionally, consideration has been given to survey for smaller limiting diameters (e.g. **2003NEOSDT**). However, such efforts have to date still been very unsucsesful: For example, in 2013, a meteoric airburst over the city of Chelyabinsk, Russia, seriously injured almost 1500 people and damaged several thousands of buildings. Although damage was limited due to the high altitude of the explosion, no precautionary measures were taken, as the asteroid was completely unknown until the moment of atmospheric entry. Luckily, such events are not a common occurrence. However, the large majority of NEA’s of this size is completely unknown, and as such they can strike anywhere at any time.

## 1.1. Near-Earth Asteroids

Asteroids are perhaps the most diverse object in the Solar system: ranging in size from tiny chips to dwarf planets such as Vesta and Ceres; from rocky compositions, to fully metallic monoliths, and composites in various elements and mineral shapes; from close to the Sun on short orbits, to distant eccentric long period trajectories. All of this greatly increases the complexity of surveying for near-Earth asteroid. Before continuing, the definition of a near-Earth asteroid will be given as follows: *a near-Earth asteroid is any asteroid with a perihelion  $q \leq 1.3\text{AU}$  and semi-major axis  $a \leq 4.2\text{AU}$ .*

Current knowledge of the asteroid population is based on past and current NEA surveys. The most important parameter to consider is the size-frequency distribution of the objects. After all, larger objects exhibit a larger impact energy and hence threat, but small objects are more common and harder to detect. A good representation for this size-frequency distribution is a power law as follows:

$$\frac{dN}{dD_p} \propto D_p^{-k} \quad (1.1)$$

With exponent  $k$  in the range of 2.95 - 3.5 (**AsteroidSizeFrequency**). Commonly, the size of the asteroid can not be directly ascertained; the target is too small to accurately determine the size. However, estimates can be made based on the absolute magnitude  $H$  of the object by relation with an assumed albedo  $p_v$  ( $p_v = 0.14$  is often used as an approximation) using the relationship first derived by **AsteroidSizeAlbedo**:

$$D = \frac{1329\text{km}}{\sqrt{p_v}} \cdot 10^{-H/5} \quad (1.2)$$

As a result of the success of the spaceguard survey efforts, past efforts have more than likely identified all NEA's with  $H \leq 15$ , corresponding to the *flying mountains* several kilometers in diameter. Also, at smaller limiting diameters, a lot of NEA's have been - and continue to be - found. The surveys through which this is achieved will be discussed in further detail in ???. Through a process of modelling the asteroid population, and simulating the performance of past surveys on it, followed by fitting the results, **GranvikPopulation** have produced a parametric model of the NEA population. The distribution of orbital elements in this model can be seen in ??.

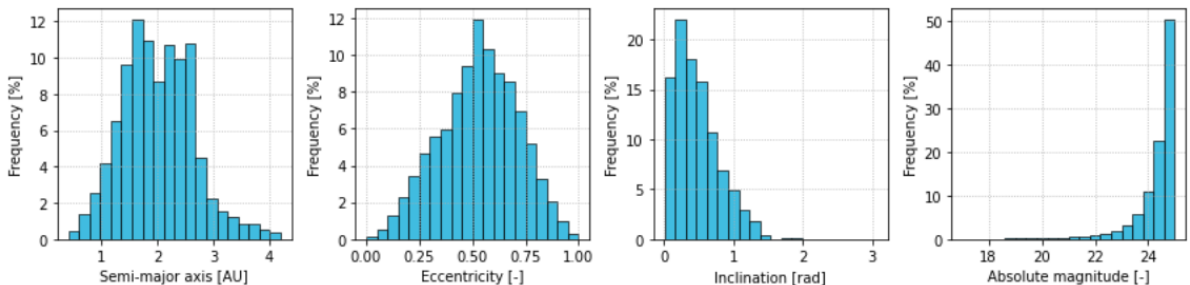


Figure 1.1: Frequency of orbital elements for modelled NEA population according to **GranvikPopulation**

Several things are of note: First and foremost, the population is very diverse; there is no particular concentration of NEA's anywhere that allows for simple exploitation in survey design. Secondly, the bulk of NEA's has a semi-major axis of  $1.0\text{AU} < a < 3.0\text{AU}$ . The dips at  $a = 2.0\text{AU}$  and  $a = 2.5\text{AU}$  correspond to the 4:1 and 3:1 orbital resonance with Jupiter, respectively. The inclination of asteroids is concentrated among the ecliptic, but very low inclinations are rare due to gravitational interactions with the planets. Lastly, the effect of ?? can be seen: 50% of the asteroids in the population generated by **GranvikPopulation** has  $24.6 \leq H < 25$ , corresponding to a diameter of  $D \leq 40\text{m}$ .

Among these small NEA's was the asteroid which entered Earth's atmosphere over Chelyabinsk in 2013. It is currently estimated that this asteroid had a diameter of 17 to 20 meters ([ChelyabinskNASA](#)). Assuming an albedo of  $p_v = 0.14$ , this would give it an absolute magnitude of  $H \approx 26.5$ . As previously discussed, completeness at these limiting diameters is very low. ?? shows the completeness as a function of size according to **HarrisPopulation**. They estimate that, at their time of writing, less than 0.005% of all asteroids of this size have been identified. Through new and continued survey efforts, **2017NEOSDT** project that the completeness at this size will increase to approximately 1.5% by 2023.

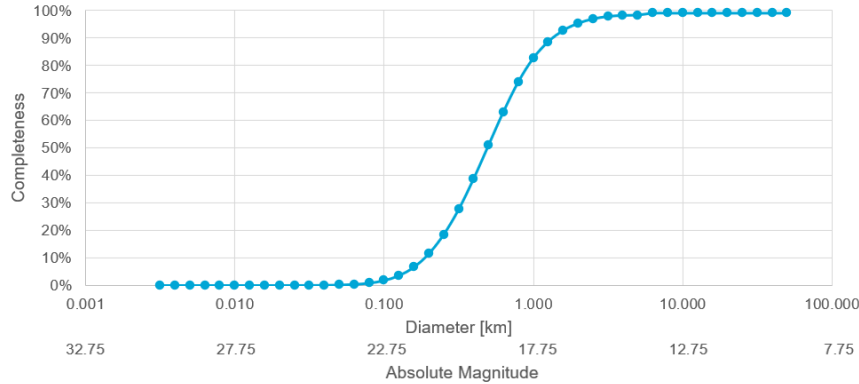


Figure 1.2: Expected survey completeness as a function of near-Earth asteroid diameter. **HarrisPopulation**

The problem can be seen in more detail in ???. Here, **HarrisPopulation** show the expected and identified population of NEA's as a function of their size. The effect of the continued spaceguard efforts can be seen clearly here: the asteroid population with  $D > 1\text{km}$  is completely known, and the population of asteroids  $D > 140\text{m}$  is nearing the targeted 90% completion. However, as the search efforts have been designed specifically to identify targets at this limiting size, the population with  $D < 100\text{m}$  is still by far and large undiscovered.

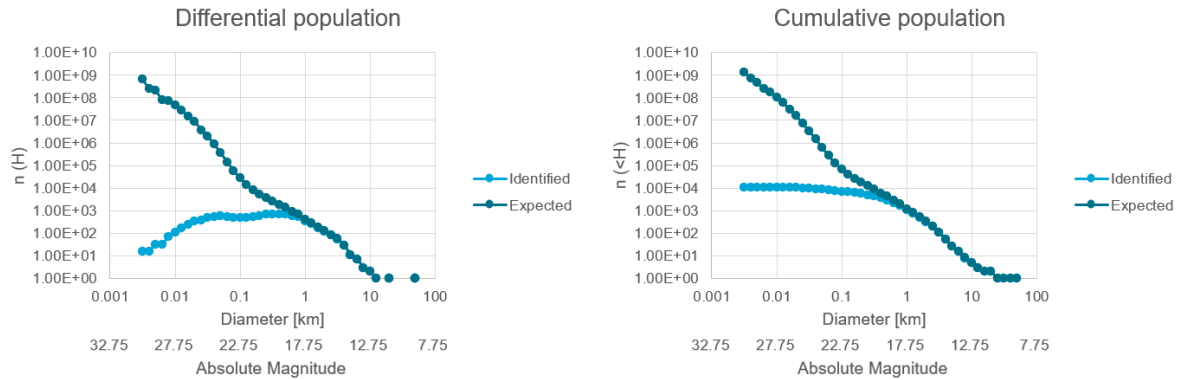


Figure 1.3: State of asteroid identification progress as of August 2014, compared to the expected number of asteroids per diameter. Note that the y-axis is logarithmic. **HarrisPopulation**

## 1.2. Past and Current Identification Efforts

Before continuing to the topic of the presented research, first some discourse shall be given to the missions that have resulted in the current knowledge of the NEA population. For brevity, not all missions will be listed; just a representative sample judged by the author to give a good overview of the state of the art. The missions are separated into two categories: space-based, and Earth-based. The latter comprises telescopes on Earth, with the advantage of having access to Earth infrastructure, supporting larger telescope apertures and providing practically unlimited electrical power, communication bandwidth, storage and computational resources. However, Earth-based systems are hindered by atmospheric distortion, extinction of light as it passes through the air, weather, limited search area depending on geographic position, and day-night cycles. Space-based systems contrast this: they are limited mostly by the maximum aperture of the telescopes they can support, the on-board processing capabilities and the computational power. Atmospheric and weather effects are mostly non-existent in space, however interference from the Sun, Earth and Moon should not be underestimated. To date, all NEA surveys from space have been carried out from orbits around Earth. Some proposals for deep space missions will be discussed in ??.

In ??, the contribution of several surveys to the total catalogue of NEAs is shown. The two largest contributors, the Catalina Sky Survey and the Pan-STARRS observatories, were both constructed to accomplish the goal of bringing the NEA survey completeness for asteroids  $D > 140m$  to over 90% of the population. The effect of these purpose-built observatories can be easily seen in their volume of discoveries. Through improvement to the facilities and processing pipelines - e.g. through better computing resources - it can be seen that the number of discoveries is still undergoing a healthy amount of growth. It is therefore important to consider the impact these surveys have on the research and proposed missions.

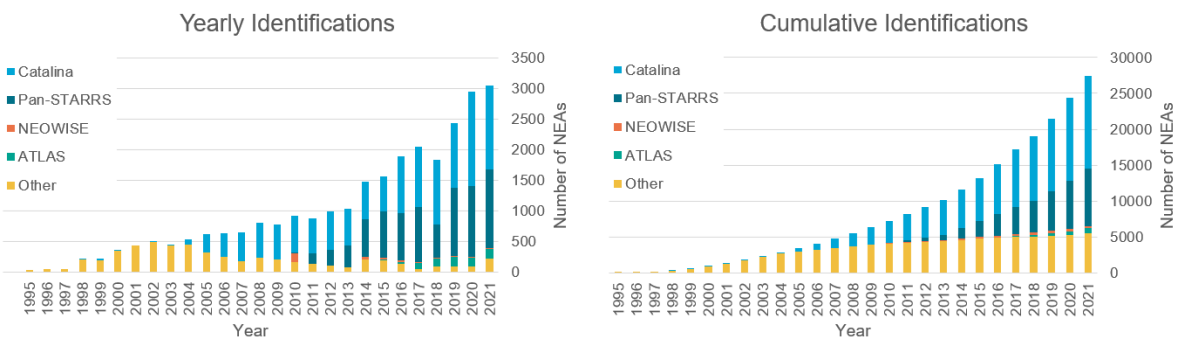


Figure 1.4: Yearly and cumulative identifications made per NEA survey from 1995 up to and including 2021. Data obtained from <https://cneos.jpl.nasa.gov/stats>

### 1.2.1. Earth-based Surveys

With almost 13000 discoveries as of the end of 2021, the Catalina Sky Survey (CSS) is currently the most successful NEA survey by volume of detections. Operated by the University of Arizona, the CSS operates a trio of telescopes in the Santa Catalina mountains: the primary telescope is a 1.5 meter wide field reflector telescope supported by a 1.0m follow-up telescope and a further 0.7m telescope, both catadioptric. The main telescope showcases the advantages of Earth-based surveys well, as it utilizes a 111 megapixel camera with a field of view of 5 square degrees. This allows it to image the sky at a very high frequency, down to a limiting magnitude of 21.5 ([CatalinaSkySurvey](#)).

The second of the major NEA surveys is the Pan-STARRS project operated by the University of Hawaii. Operating two 1.8m catadioptric telescopes, equipped with 1.4 gigapixels camera sensors, it is capable of imaging down to a visual magnitude of 24. Currently, development is underway to expand Pan-STARRS to four telescopes, and allowing it to serve as a precursor for development of the software and data processing of the Large Synoptic Survey Telescope, which will be further discussed below ([PANSTARRS](#)).

The last of the current large NEA surveys is the ATLAS (Asteroid Terrestrial-Impact Last Alert System) project. Contrary to the previously mentioned surveys, the goal of ATLAS is not to catalogue large quantities of NEAs, but to provide a last warning in case of incoming impactors. It is comprised of two 0.5m catadioptric telescopes, with plans to expand the system with three more sets of two telescopes. The survey is completely automated, and is tasked with providing impact warning for targets too small to impact until their last approach. The predicted warning times are between a day and a week (**ATLAS**). Although this allows for alleviation of some of the damage, it is too short to take significant countermeasures such as an asteroid deflection mission or a large-scale evacuation. In addition, ATLAS suffers from the same problems as other Earth-based telescopes. For example, the 2013 Chelyabinsk meteor was not detected, as it approached Earth from the direction of the Sun.

Although not yet in operation, the expected impact of the Large Synoptic Survey Telescope (LSST) warrants a mention. Currently being constructed in the mountains of Chile, the LSST will utilize a three-mirror reflector with a 8.4m aperture, in combination with a 3.2 gigapixel sensor, making it the largest digital camera ever produced. It is expected to enter operations fully in October 2023, with a limiting magnitude of around 24.5 (**LSST**). Although the LSST is expected to complete the goal of cataloguing 90% of the  $D > 140\text{m}$  NEA population in approximately 12 years, it can be seen from its limiting magnitude that detecting the faintest of NEAs will not be a successful endeavor for an Earth-based survey, even at extreme apertures and sensor sizes. Therefore, a short overview of some space-based surveys will now be provided.

### 1.2.2. Space-based Surveys

As shown above, meaningfully increasing the survey completeness for asteroids under the  $D > 140\text{m}$  threshold is best carried out by means of a survey from space. To date, no dedicated NEA survey spacecraft has been launched, however, several missions have discovered a significant number of NEAs, most prominently among those the NEOWISE mission. Initially used for the WISE mission, imaging the entire sky in near-infrared, the spacecraft was put into hibernation after the coolant for its camera sensor ran out. In 2013, it was reawakened for the NEOWISE mission, where it would use its sensors in a non-cryogenic mode to survey for NEAs. Although the number of NEAs detected by NEOWISE is small compared to the dedicated Earth-based surveys, the new objects detected by it have been small and dark: targets which are hard to impossible to image using visual telescopes from Earth (**NEOWISEResult**). NEOWISE thereby has shown the capability of both a space-based survey and a survey using near-infrared sensors, and its findings have contributed greatly to the capabilities for modelling the NEA population (e.g. **GranvikPopulation**).

Building on the success of NEOWISE, a new spacecraft is currently being developed by NASA under the NEOCam project. Aiming for a launch in 2026, the NEOCam mission has a dedicated design for identification of NEAs. Situated at the Sun-Earth L1 point, the mission will observe the space around Earth for potentially hazardous asteroids. It is expected that NEOCam is also capable of completing the 90% survey completeness of asteroids  $D > 140\text{m}$ , and will be capable of imaging some asteroids down to  $D > 30\text{m}$ , although the latter is not a primary design goal (**NEOCam**).

## 1.3. Novel Proposals

As an update to the new spaceguard objective, **DefendingEarth** investigated the progress and goals of NEA cataloguing efforts. Their initial verdict was that current survey efforts are insufficient to meet the new goal, and new missions will be necessary. Several of these surveys have already been discussed above. However, next to discussing NEAs with  $D > 140\text{m}$ , they also state that “*... objects smaller than 140 meters in diameter are also capable of causing significant damage to Earth.*” and make the recommendation that “*Because recent studies of meteor airbursts have suggested that near-earth objects as small as 30 to 50 meters in diameter could be highly destructive, surveys should attempt to detect as many 30- to 50-meter objects as possible.*”

Leading among the current proposals is the work by NASA's Jet Propulsion Laboratory (**2003NEOSDT**, **2017NEOSDT**). The initial proposal centered around updating the limiting size of to-be-detected asteroids to lower limiting diameters. The authors investigate a multitude of possibilities for accomplishing the 90% completeness at  $D > 140\text{m}$  goal, as well as investigating the influence on smaller diameter asteroids. Their conclusion is in line with the aforementioned: the most promising option for cataloguing a multitude of NEA's is to perform a survey from deep space. Several options are considered, among which the best performing options are 0.5 meter aperture thermal infrared telescopes at Earth-Sun L1 or in Venus-trailing orbit. The authors note no significant gain in performance by sizing up the telescope. It is also noted that no full optimization for the orbit or payload is performed. However, the proposal shows a lot of potential.

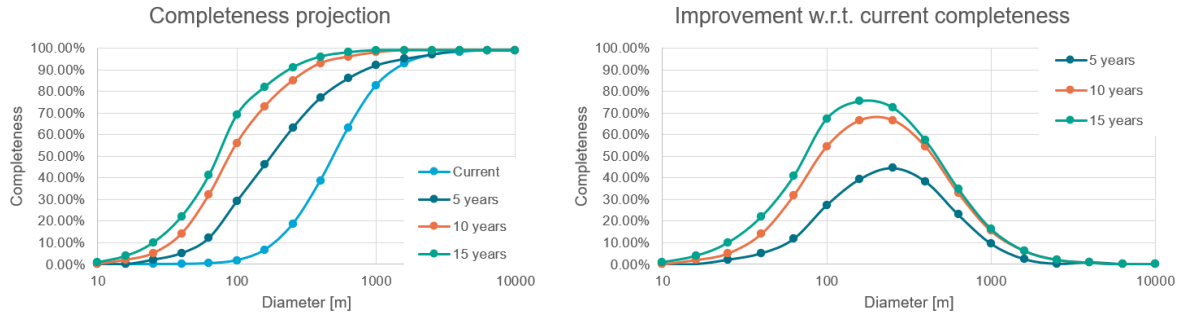


Figure 1.5: Projected improvement in survey completeness for a 5, 10 and 15 year survey from deep space. Data from **2017NEOSDT**.

?? shows a projection for the improvement in survey completeness as a function of NEA diameter for a hypothetical deep space survey. A few thing are of note: Firstly, it is clear that such a survey can offer a sizeable improvement in cataloguing efforts, additionally leading to completion of the spaceguard goal in several years. However, several of the aforementioned missions currently under development also have this potential. What is more interesting is that, due to the thermal infrared telescope, cooled in deep space and largely free from interference by planets, is likely to detect a large number of small NEAs, which was hinted at by the success of the NEOWISE mission. But, the main bulk of the improvement is found in the  $100\text{m} < D < 1000\text{m}$  range. Lastly, the diminishing returns of running a mission for longer become clear: as the number of undetected NEAs which fall within the limiting magnitude of the detector decreases, the performance decreases with it.

A second proposal among deep space surveys is the work of **ThesisOlga**. Her work investigates the problem of asteroid impact last warning from space. This addresses the weakness in systems such as ATLAS which was showcased by the Chelyabinsk impactor: If an asteroid approaches Earth from the Sun, it is not possible to detect it in advance from Earth, as the glare of the Sun will overpower the signal of the asteroid. **ThesisOlga** shows that a system at the solar sail displaced Sun-Earth L1 point will provide good improvement to the effort of asteroid impact last warning strategies. However, as previously discussed, this would still leave insufficient time for e.g. a deflection mission (for the interested reader, **DefendingEarth** gives a good overview of mitigation strategies). In addition, although the performance is vastly increased, performance in detecting asteroids coming from the direction of the Sun is still limited.

From the above, it is clear that current efforts are insufficient to reach the set goals for NEA cataloguing. In addition, although future surveys will reach this goal, they will only detect a small fraction of small NEAs, not cataloguing the largest population of near-Earth objects. In fact, even proposed surveys which avoid all interference from the atmosphere, the Earth and the Moon will not be capable of reaching this goal with a single spacecraft. Limitations are imposed by the location of the spacecraft, the required number of observations, and interference from Solar glare.

# 2

## Research Outline

In ??, some background on the difficulties of identification and cataloguing of NEAs was given. In this chapter, the resulting problem and associated knowledge gap will be presented. Then, the associated research questions and expected outcomes will be listed.

### 2.1. Problem Statement

Currently, humanity's knowledge of NEA populations is at a low level of completeness, especially for small diameter NEAs. Therefore, valuable scientific knowledge about the composition and evolution of the Solar system is unknown, and Earth is vulnerable to impacts which can be hazardous to human life and property.

It has been shown that current efforts are not adequate to reach the current goal of the spaceguard survey. Several missions have been proposed, and others are under development, which will cover this goal. However, a new more ambitious goal to identify smaller NEAs is still far out of reach. Even with a modern satellite positioned in deep space, only a limited survey completeness can be reached at limiting diameters  $D < 100\text{m}$ . This is caused by the limitations in position of this system, the required follow-up time and the number of detections required, and interference from the Sun.

### 2.2. A Multi-Spacecraft Approach

To address this problem, we propose the option of a multi-spacecraft system. In recent years, spacecraft constellations have already shown a lot of potential in reaching complex mission goals. In the application of near-Earth asteroid surveys, more telescopes will firstly speed up the survey cadence, allowing the system to image the same area of sky at a faster rate. However, there are further synergistic advantages to such an approach. Three major benefits are noted in a multi-spacecraft system over a single telescope, which will be discussed in the following paragraphs.

Firstly, a multi-spacecraft system will mostly solve the problem of Solar glare: Although a spacecraft in syzygy with the Sun and an asteroid will not be able to detect the latter if it is located in the direction of the Sun, a different spacecraft located away from it might observe the Sun-asteroid arrangement from the side, allowing it to detect the target. In this way, a multi-spacecraft system is capable of minimizing the amount of blind spots in the search space. ?? shows a visualisation of the reduction in blind areas when adding an additional spacecraft.

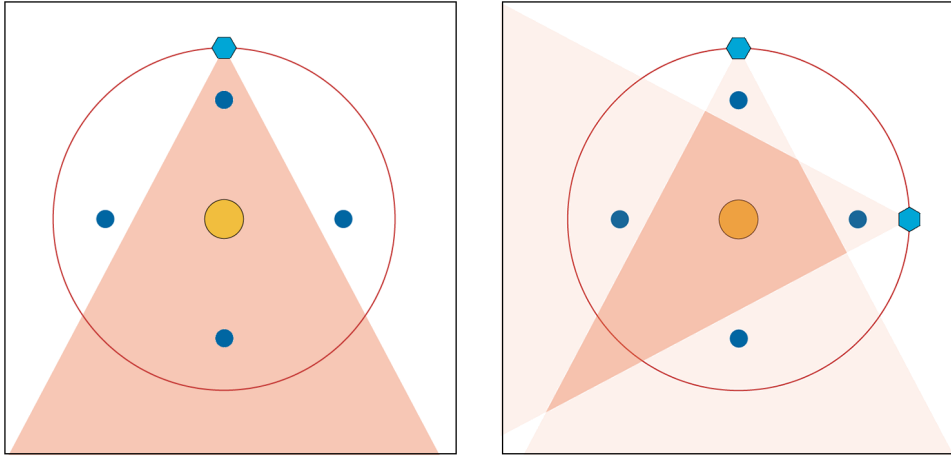


Figure 2.1: Consider a spacecraft (represented by the cyan hexagon) attempting to observe several asteroids (blue circles). Because of Solar glare and thermal limits (red-shaded area), the spacecraft is unable to observe the top and bottom NEA. However, addition of a second spacecraft greatly reduces the “blind area”: now the system can observe all four NEAs.

Secondly, using multiple spacecraft allows for easier identification and orbit determination of the NEA: Normally, a single telescope takes images in 2D of a target. As the asteroid will almost certainly be below the Rayleigh criterion of the telescope, it is not possible to estimate how close the asteroid is from its estimated diameter and the projected size on the sensor. Therefore, only the angular direction towards the target is known. Therefore, to obtain the orbit of the target requires solving Gauss’ problem, which requires a minimum of three subsequent observations (six unknown parameters for the full orbit specification, two variables measured per observation). When using multiple spacecraft, it is possible to perform a kind of “triangulation”, provided the spacecraft and the asteroid are not colinear. This allows for solving for the three-dimensional position of the asteroid. Thus, using only two observations in time reduces the orbit determination to Lambert’s problem. This means the asteroid will only have to be within the area where telescopes can observe it for half the time as a single-spacecraft system. This is further shown in ??, where addition of a second spacecraft allows for observing the asteroid before it moves out of the observable range.

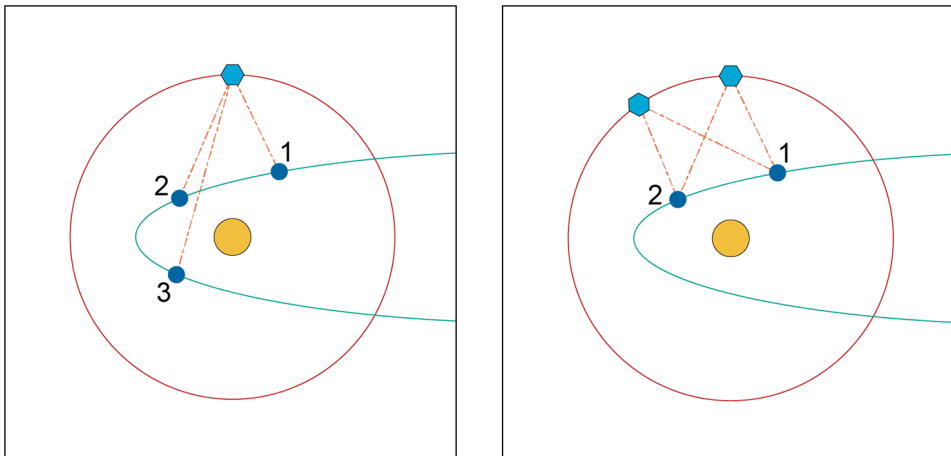


Figure 2.2: Normally, in order to perform orbit determination, the spacecraft (cyan hexagon) would have to image a target (blue circle) three times. For targets that are hard to observe, such as a highly eccentric NEA which can only be detected close to perihelion, this leads to problems: the third detection will be hard to obtain, as the NEA moves behind the Sun into the blind area, or out of the detector’s range altogether. Addition of a second spacecraft allows triangulation, thus halving the time required to identify the asteroid, performing the necessary measurements before the asteroid moves far away again.

Lastly, a multi-spacecraft approach allows for more complex search strategies. The possibility for doing such search strategies when multiple sensors are available is demonstrated by the Catalina Sky Survey. Using their follow-up telescope, a new target is quickly selected for follow-up imaging, quickly gathering the required observations to perform orbit determination and thereby identification. In space, such a strategy would of course be more complex, as the problem becomes influenced by the location of the spacecraft. However, such an implementation will be very helpful in detecting NEAs which are only visible for a short period of time, such as highly eccentric objects with long semi-major axis, which are only visible for a short window around their perihelion. This idea is demonstrated in ??.

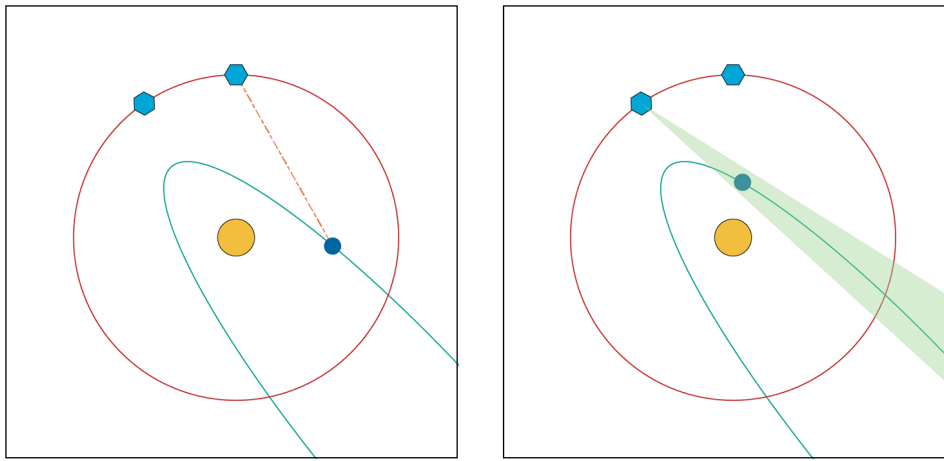


Figure 2.3: In a more advanced system, some of the spacecraft could be dedicated to follow-up observations. As soon as one spacecraft detects a target, the second spacecraft is instructed to point in the direction of the new observation. In that way, even if a target is only observable for a short period, the spacecraft will have a much larger chance of pointing towards it.

However, before such strategies can be developed and implemented in a mission, it is first required to know the location and composition of such a multi-spacecraft system. To the author's best knowledge, the behavior of a multi-spacecraft survey has never been evaluated. In addition, to adequately assess the performance, it is vital to discover where the craft in such a system should be positioned, and how they should be equipped. The aim of this work are to provide insight into these points using simulation of such a survey.

### 2.3. Research Questions and Expected Outcomes

To translate the aim into a concrete research topic, a main research question and a set of derived subquestions is composed. The main research question is:

#### **What is the optimal position and composition for a system of spacecraft with the purpose of identifying and cataloguing previously unidentified near-Earth asteroids?**

A few terms deserve special attention: To begin, the terms *position* and *composition* serve to indicate the scope of the research. As mentioned previously, no previous work has been published on multi-spacecraft NEA surveys. The current body of work on space-based surveys commonly uses general categories of orbits such as Venus-trailing orbits, or orbits at Lagrange points. In addition, either thermal infrared or a visual light telescope is used. In a multi-spacecraft system, the position should be treated in a more general sense: there is the added element of combining different positions synergistically, as explained in the previous section. Also, the composition with regards to payload is worthy of investigation: perhaps, a synergistic combination of slower but more sensitive infrared and faster but less sensitive visual light telescopes might be of merit. In addition to specifying what should be researched, these terms also limit the scope: other aspects, including - but not limited to - search strategy, communication between spacecraft, and image processing techniques will be left to further research.

The second factor of note is *identifying and cataloguing*. The distinction between observation, detection, identification and cataloguing is worth the discourse before continuing. Essentially, these terms all represent successive steps in the survey. An *observation* is when a target is within the telescope's field of view when an image is taken. Of course, this is not useful in and of itself. Therefore, a *detection* can be established when the signal-to-noise ratio of the asteroid in the image is sufficiently high. At this point, it is clear that "something" is present in the telescope's field of view. When enough detections are established within a certain time frame, it becomes possible to determine the orbit of the target, and to see whether or not it is already known. At this point, an *identification* can be performed from the subsequent observations. Then, with the orbit of the target known, the survey can proceed to *cataloguing* the NEA by transmitting the relevant data back to Earth for analysis and storage. Thus, it is apparent that just observing or detecting an NEA is not useful in and of itself. For the information to be relevant, the system should be capable of assisting in the identification and cataloguing efforts.

The last term important to give some discourse to before further explaining the research is *unidentified* asteroids. As was discussed in ??, humanity has already catalogued a sizeable portion of the NEA population. Of course, it is not necessary to identify these targets again. Therefore, the research effort should be concentrated on solving the identified problem of improving the knowledge of the small-diameter NEA population.

In support of the main research question, in conjunction with the aim of addressing the problem through a numerical simulation, several subquestions were drafted to assist in providing an answer. The first three subquestions are related to the design of the simulation; how to accurately produce and operate a model of NEA surveys. The next three questions are related to the parameters of such missions; where the spacecraft are located and how the system is composed. Lastly, a subquestion is included which will be essential for judging the results in the context of current and future endeavors, such as those listed in ?? and ?. The subquestions are explained in brief below:

1. **How can the population of NEAs be accurately modelled, and how can these models be adjusted for unidentified NEA's?**: The first subquestion is related to simulation. As mentioned above, the model needs to give an accurate estimate for how the system will perform in surveying unidentified NEA's. Therefore, first a model of this population is required. Although this may seem straightforward, it might pose some challenges: after all, only the identified portion of the NEA population is known, the unidentified portion is clearly not. Fortunately, literature sources are available to assist in this process.
2. **How can surveys of NEA's by a system of spacecraft be accurately modelled?**: Having the asteroid population, the next consideration is how to model a survey of that population. Again, good sources in literature are available to assist in solving this question, although sufficient verification and validation will need to be performed.
3. **How can the position and composition of the system be optimized?**: Already mentioned above, the possibilities for positioning and composing a multi-spacecraft system grow exponentially with the number of spacecraft in the system. Therefore, a good method of optimizing the system is required. It is expected that the simulation will be computationally expensive, and possibly noisy. Therefore, selection of a proper optimization method is crucial to ensure good results.
4. **What is the effect of increasing the number of spacecraft on the process and performance of identifying and cataloguing NEA's?**: The first question related to the behavior of the system, and probably the most straightforward relation to consider when looking at the research question. Although it is apparent that an increase in the number of spacecraft will always increase the performance (or at worst, have it stay constant), the number of spacecraft is the most relevant free parameter to have results on, as it is a very important concept to explore and consider for future missions.
5. **How is the performance of possible payload compositions affected by the number of spacecraft, and what is the resulting optimal payload composition?**: Secondly, the payload of the system. As explained in ??, current research often uses either a visual or a thermal infrared telescope. However, when considering a multi-spacecraft system, combinations of these are possible. It will be good to see which of the systems benefits mostly from the increase in the number of spacecraft, and whether synergistic effects occur in "hybrid" systems composed of a mix of instrumentation.

6. **How do the number of spacecraft and payload interact with the orbital parameters of the system?**: The last of the free parameters, the positioning of the spacecraft. Although it is not very crucial for the preliminary stage of mission design which is the target of this mission, it is important to understand what the interaction between these factors is and how this affects the performance.
7. **How effective is a system of multiple spacecraft at identifying and cataloguing previously unidentified NEA's compared to other current and future methods?**: A multi-spacecraft survey mission is a very costly endeavor, requiring several expensive spacecraft and vehicles for launching these into outer space. Although this work will not go into detail on the economics of space missions, a realistic assessment to the merits of the idea should be made to consider whether it would be worth it to develop such a mission.

It is expected that through answering this research question, several outcomes will be obtained. The main goal is to provide outcomes which are useful in doing further research into, as well as designing, future NEA survey missions. The desired outcomes of this work are thus as follows:

1. Understanding how increasing the number of spacecraft affects the performance of a NEA system. Of course, the performance will increase, however the main interest is in how much this performance increases, and thus whether such a solution is worth considering for future missions. It is expected that in addition to this, insight will be gained into any diminishing returns for higher numbers of spacecraft, and perhaps limits beyond which adding additional spacecraft provides no tangible benefit anymore.
2. A conclusion on where to focus efforts with regards to payload. Currently, thermal infrared telescopes are considered the best choice for future NEA missions (e.g. [2017NEOSDT](#), [ThesisOlga](#)). However, perhaps the benefits of a multi-spacecraft system are expressed stronger in a visual light system, or a hybrid system might provide a synergistic benefit.
3. Insight into changes to the optimal orbital position for the spacecraft as a function of the number of spacecraft. It is expected that these quantities will undergo some change, and mapping this out allows for relating the results to the results of other studies on where to position NEA survey spacecraft.
4. Reliable estimates for what performance to expect as a higher number of spacecraft is utilized in the system. In addition, this result is also interesting in reverse: seeing what kind of system would be necessary to obtain a desired result provides a basis for designing a mission out of such a requirement.

Through fulfilling these goals and providing the expected outcomes, a useful base for further work on these kind of NEA surveys will thus be laid.



# 3

## Survey Modelling

Space missions are very expensive to design, build, launch and operate. Therefore, it is important that all properties and behaviors of such a mission are well known in advance. Then, an accurate assessment can be made of the merits of the mission and what results are to be expected. In addition, it allows for selecting the design which will produce the best results. In order to study these properties and determine the optimum, computer simulations are an excellent tool. They allow for cheaply and rapidly testing out a lot of possible mission parameters, and recording the relevant data for easy analysis.

Currently, no model is publicly available for modelling multi-spacecraft surveys. Therefore, a simulation will be developed. During and after development, the model is also extensively verified and validated. The process for this is described in REF<sup>??</sup>. Other research (e.g. **Flyeye**, **2017NEOSDT**) has demonstrated the potential for explicitly modelling out the entire survey as it would be conducted by the actual system. In this chapter, the theoretical background for the various steps in simulating a NEA survey will be given. Implementation of the simulation will then be treated in the next chapter.

The components of the simulation consist of first generating a representative population of asteroids (described in ??), then, at each timestep, calculating the background and target signal (?? and ??, respectively). Knowing these signals, the signal-to-noise ratios can then be determined after estimation of some of the detector properties (??). The frequency and location of the observations is determined by the search strategy, and resulting cadence (detailed in ??) and lastly through repeat observations, it can be determined whether the system is capable of identifying a target (??).

### 3.1. Population of Asteroids

The first component of the simulation is the asteroid population model. This population was already briefly described in ?? . In this section, more details on the generation of the population and the process of determining the positions of the NEA's, are given. As already mentioned in ??, the most comprehensive debiased population model is the one by **GranvikPopulation**. This population model was generated by propagating an initial population of NEA's based on several known interactions (e.g. gravitational interaction with the planets), and then comparing the resulting population to the results of the NEOWISE mission. Essentially, the problem then reduces to the question: "What initial population would result in the results that are observed in the NEOWISE mission?". Then, the initial population model can be fitted to the results of the NEOWISE mission, and a debiased population model is thus obtained.



Figure 3.1: Distribution of the full population of asteroids per **GranvikPopulation**, and an estimation of how many asteroids have already been identified, per **HarrisPopulation**. The left graph is shown logarithmically, the right graph linear.

Of course, this results in a full population of NEA's; whereas a population of *unidentified* NEA's is required for this work. Therefore, a correction to the population was made based on the work of **HarrisPopulation**. To do this, the population as given by **GranvikPopulation** was separated, based on absolute magnitude, into bins of width 0.5. Then, it was assumed that the detection of NEAs is roughly uniform over the orbital parameters. The completeness statistics of **HarrisPopulation** can then be used to discard a part of the population as *identified*. This is shown in ???. Of course, the assumption of uniformity in the detection of NEA's is false: highly eccentric NEA's, NEA's that are very dark, or NEA's with a long semi-major axis are more likely to be undetected. However, no data is available on this matter, and therefore no better alternative was deemed to be available. As all simulations will be affected equally, and in addition, as can be seen in the second diagram in ???, only a small part of asteroids is discarded - the largest population groups by size have very low completeness numbers - the error is judged to be sufficiently small for practical purposes.

### 3.2. Background Signal

Before considering the existing knowledge on modelling asteroid signals, first the background in which these targets has to be observed is discussed. In this section, the current relevant body of knowledge on modelling this background signal will be listed. The background signal will be split into two components. Firstly, the background light originating from the Sun. This manifests most dramatically in the form of direct sunlight. However, also reflections off of interplanetary dust are important. This reflection manifests in the phenomena of zodiacal light and gegenschein. The second component of the background signal, is the light from outside the Solar system. This light originates from other stars and manifests mainly as a diffuse background of starlight. Particularly, a very large concentration of this starlight is found around the galactic plane.

The reason for separating the background signal into these two components is straightforward: in a reference frame fixed among the stars, the background signal from outside the Solar system is practically unchanging as the spacecraft moves around the Sun; the parallax of moving several AU is negligible on galactic scales. In contrast, the contribution of light from our Sun is directly dependent on the position of the spacecraft with regards to the Sun. In the following sections, two primary reference frames are used: a heliocentric ecliptic reference frame (A right-handed reference frame whose principal plane is the ecliptic plane, origin at the center of the Sun, and the positive X-direction towards the vernal equinox), and a galactic reference frame (A right-handed reference frame whose principal plane is the plane of the Milky Way, origin at the center of the Sun, and positive X-direction towards the galactic core). The transformations between ecliptic longitude and latitude ( $l_e, b_e$ ) and galactic longitude and latitude ( $l_g, b_g$ ) are as follows:

$$b_g = \sin^{-1}(\sin b_e * \sin B_{NGP}) - \cos b_e \sin b_{NGP} \sin(l_e - l_{NGP}) \quad (3.1)$$

$$\sin l'_g = \frac{\sin b_e \cos b_{NGP} + \cos b_e \sin b_{NGP} \sin(l_e - l_{NGP})}{\cos b_g} \quad (3.2)$$

$$\cos l'_g = \frac{\cos(l_e - l_{NGP}) \cos b_e}{\cos b_g} \quad (3.3)$$

$$l_g = \begin{cases} \sin^{-1}(\sin l'_g) + l_{GC}; & \cos l'_g \geq 0 \\ \pi - \sin^{-1}(\sin l'_g) + l_{GC}; & \cos l'_g < 0, \sin l'_g > 0 \\ -\pi - \sin^{-1}(\sin l'_g) + l_{GC}; & \cos l'_g < 0, \sin l'_g \leq 0 \end{cases} \quad (3.4)$$

With  $b_{NGP}$  the latitude of the North Galactic Pole, approximately equal to  $29.81^\circ$  or  $0.5203$  rad; ascending node of the Galaxy  $l_{NGP}$ , approximately  $270.02^\circ$ ,  $4.712$  rad; and longitude of the galactic core  $l_{GC}$ , approximately  $6.38^\circ$ , or  $0.1114$  rad. Finally, a transformation is required to express the ecliptic coordinates in a frame which is relative to the Sun, as the Sun-based contribution will be expressed relative to the Sun. This is however simply a subtraction of the latitude  $l_e^\odot$  and longitude  $b_e^\odot$  of the Sun in the ecliptic frame, from the latitude and longitude of the target in the ecliptic frame:

$$l_h = l_e - l_e^\odot \quad (3.5)$$

$$b_h = b_e - b_e^\odot \quad (3.6)$$

With the reference frames defined, the individual components can be discussed. Firstly, the contribution of the Sun will be discussed, and then the background starlight for both thermal infrared and visual light.

### 3.2.1. Solar contribution

Modelling of the thermal infrared background radiation as a result of the light from the Sun is described by **IRDust**, based on observations of the COBE mission. This model focusses on a modelling of the thermal state of interplanetary dust, and the resulting thermal infrared emission observed. Thus, the signal is not comprised of light originating at the Sun - but rather on the radiation from bodies heated by that light. The authors state that the albedo of particles at the relevant wavelengths is very close to zero, and therefore scattered Sunlight need not be considered; only the emissions of the particles. Thus, the zodiacal flux  $Z(l, b)$  can be expressed as an integral over the line of sight (in practice, a distance up approximately the orbit of Jupiter is sufficient) of the sensor of the various contributions (which will be discussed in more detail below):

$$Z(l, b) = \Sigma_c \int_{\lambda_0}^{\lambda_1} \int_S n_c(X, Y, Z) E_c(\lambda) B(\lambda, T) ds d\lambda \quad (3.7)$$

With  $n_c$  being the density of the dust due to a contribution  $c$ ,  $B$  is the blackbody emission given by Planck's law and  $E_c$  is a wavelength-specific emission correction factor. The temperature of the dust grains is assumed to follow a power law function of distance from the Sun  $R$ :

$$T(R) = T_0 R^{-0.467} \quad (3.8)$$

Temperature  $T_0$  at 1 AU is set to 286 K, and the emissivity modifications at the  $4.9 \mu\text{m}$  and  $12 \mu\text{m}$  thermal infrared wavelength are 0.997 and 0.958, respectively. Then, based on observations of the COBE mission, the authors construct a parametric model, based on three contributions. The first contribution is a "donut-shaped" dust cloud centered on the Sun, and inclined  $2.03^\circ$  with respect to the ecliptic. This is the largest contributor to the density of interplanetary dust. Two more contributions which are modelled are a set of three dust bands, inclined at  $0.56^\circ$ ,  $1.2^\circ$  and  $0.8^\circ$ . Lastly, a circumsolar ring is modelled along the orbit of the Earth, which has a higher concentration around  $10^\circ$  behind Earth in its orbit, as dust trails the planet due to its gravity. For conciseness, the exact model will not be described here in detail; interested readers can refer to **IRDust**. An illustration of the contours of the components is seen in ??.

The combined density model is shown in ?? . As can be seen, the dust cloud is the largest contributor to the density of the dust cloud. With the density and temperature components known, the infrared background due to the interplanetary dust can be modelled. The only factor that needs to be added to this is the direct thermal radiation from the Sun, which can be obtained directly from Planck's law.

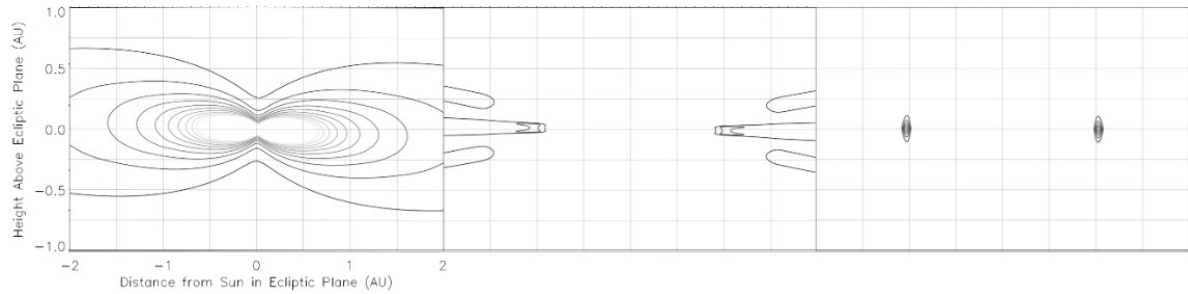


Figure 3.2: Isodensity contours of the interplanetary dust model, shown at a plane perpendicular to the ecliptic. F.l.t.r.: the dust cloud, dust bands, and the circumsolar ring. Units of the contours are  $10^{-7} \text{ AU}^{-1}$  for the dust cloud, and  $0.125 \cdot 10^{-7} \text{ AU}^{-1}$  for the bands and ring.

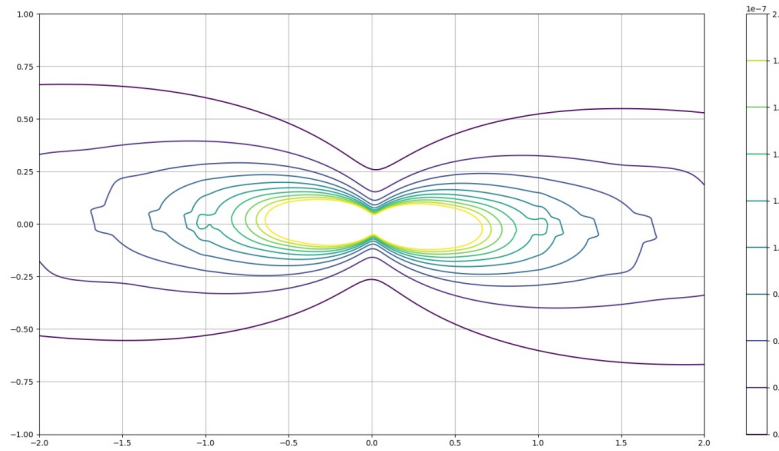


Figure 3.3: Combined isodensity contour of the interplanetary dust in a plane perpendicular to the ecliptic. TO DO: 3D PLOT

Combining all these components and performing the integration leads to the full contribution as a result of Solar radiation and interplanetary dust. An illustration of the signal can be seen in ???. The contribution from the Sun, and the hot dust near the Sun, is the most important source. However, there is still a sizeable flux originating in the interplanetary dust throughout the Solar system.

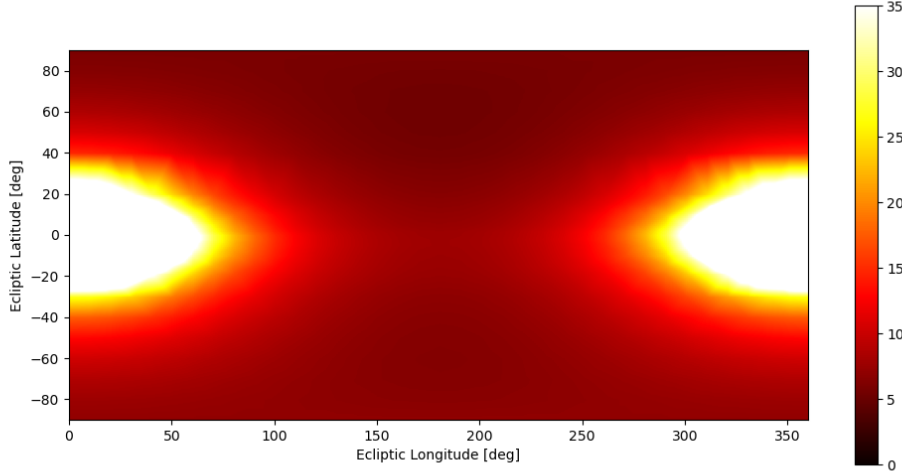


Figure 3.4: Contribution of light from the Sun to the background signal in thermal infrared, in ecliptic coordinates, as seen from a spacecraft located at  $(-1, 0, 0)$  AU. Units are Megajansky per steradian,  $1 \text{ MJy sr}^{-1} = 10^{-21} \text{ W m}^{-2} \text{ Hz}^{-1} \text{ Sr}^{-1}$ , and the scale is clipped at  $35 \text{ MJy sr}^{-1}$  for clarity.

On the other hand, the background signal in the visual spectrum is more readily available. As it can be quickly and repeatedly measured from the surface of the Earth, early measurements of this signal exist. The components of the visual light background signal are tabulated by **LightOfTheNightSky**, using data obtained from measurements. The resulting contribution from the Sun and Sunlight reflected off of interplanetary dust can be seen in ???. Next to the obvious contribution of the Sun and zodiacal light, the phenomenon of gegenschein can be observed in the middle of the plot. Although this is the point where target asteroids are at their brightest, it is also a point of increased background flux. The values as tabulated by **LightOfTheNightSky** are only valid at a distance from the Sun of 1 AU. **SkyBrightness** offer a correction factor for changing heliocentric position of the observer as follows:

$$F(R) = F_{1 \text{ AU}} R^{-2.3} \quad (3.9)$$

This correction factor accounts for both the approximate decrease in interplanetary dust density when moving away from the Sun, as well as the decrease in solar flux. With these components, the Sun-dependent portion of the background signal is fully available for modelling.

### 3.2.2. Milky Way and Diffuse Starlight

For the background signal originating from the Milky Way and other diffuse starlight, similar models exist for both the thermal and infrared and the visual light spectrum. By subtraction of the signal from the Sun, zodiacal light and gegenschein, the remaining portion of the background signal could be attributed to this component. The resulting models from **IRDust** and **LightOfTheNightSky** are shown in ?? and ??, respectively. Due to the research being more modern, and more computer and data storage resources being available at the time, the thermal infrared background model can be seen to be more detailed than the visual light spectrum model. However, other similarities, such as the light from the galactic core around  $l_e = 270^\circ$  can be observed in either. Lastly, note that while the diffuse background starlight generally has a lower magnitude than the emission and reflection of the interplanetary dust, the Milky Way is brighter than the interplanetary dust in both spectra and thus warrants inclusion into the model.

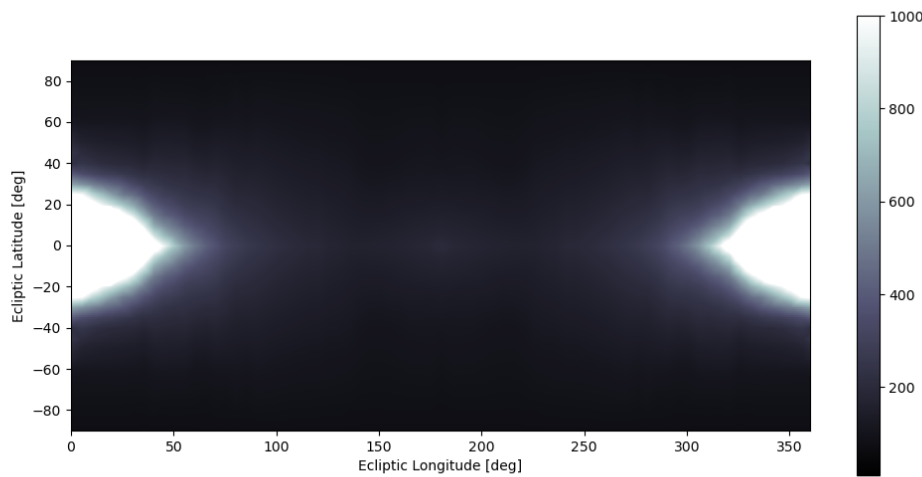


Figure 3.5: Contribution of light from the Sun to the background signal in the visual spectrum, in ecliptic coordinates, as seen from a spacecraft located at  $(-1, 0, 0)$  AU. Units are  $S10_{\odot}$  or solar-type stars of 10th magnitude per square degree.  $1 S10_{\odot} = 9.00 \text{ W m}^{-2} \text{ Sr}^{-1}$ . The scale is clipped at 1000  $S10_{\odot}$  for clarity.

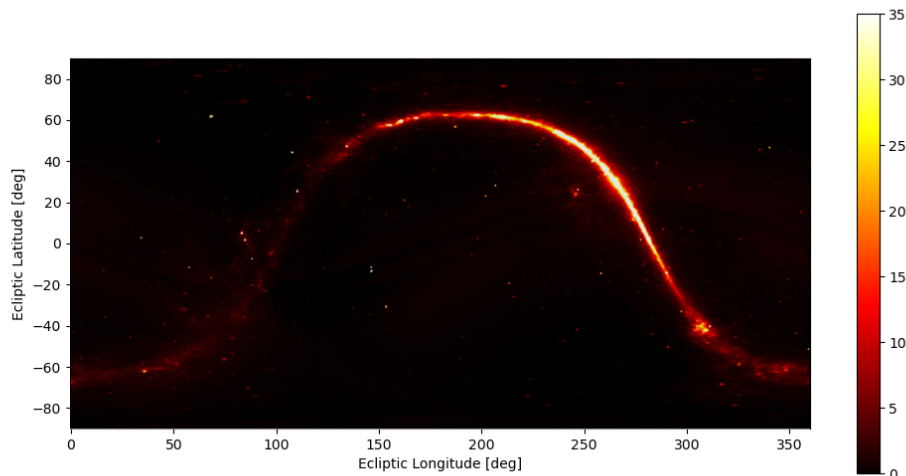


Figure 3.6: Contribution of light from the Milky Way and diffuse starlight to the background signal in thermal infrared, in ecliptic coordinates. Units are Megajansky per steradian,  $1 \text{ MJy sr}^{-1} = 10^{-21} \text{ W m}^{-2} \text{ Hz}^{-1} \text{ Sr}^{-1}$ , and the scale is clipped at  $35 \text{ MJy sr}^{-1}$  for clarity.

A final note is to be made about individual stars: readers who occasionally glance at the night sky are undoubtedly familiar with the fact that numerous stars outshine the diffuse background, making them appear as individual, distinct points. Naturally, these points will also appear in images taken of the sky. However, as these objects are essentially fixed with regards to the movement and timescale of human surveying efforts, they have been extensively catalogued. Therefore, removal of these points is a fairly straightforward and well-understood process (see **StarRemoval** for a thorough explanation of the process), and they can be let out of the modelling effort without affecting the results.

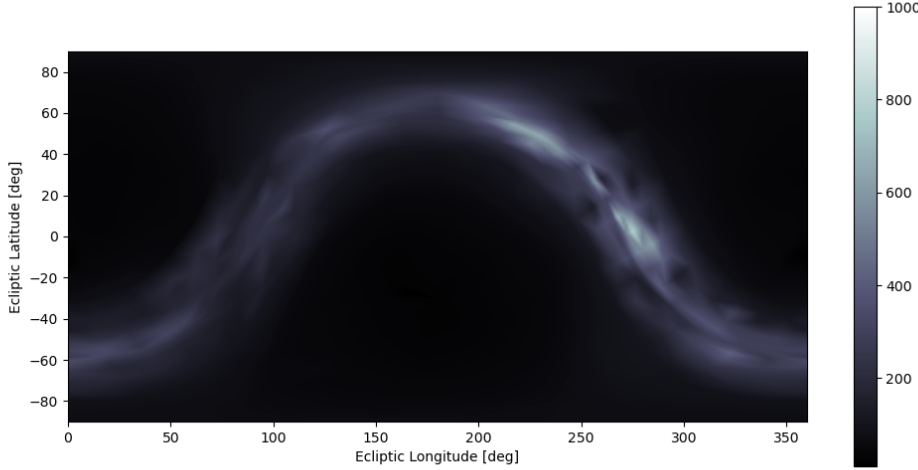


Figure 3.7: Contribution of light from the Milky Way and diffuse starlight to the background signal in the visual spectrum, in ecliptic coordinates. Units are  $S10_{\odot}$  or solar-type stars of 10th magnitude per square degree.  $1 S10_{\odot} = 9.00 \text{ W m}^{-2} \text{ Sr}^{-1}$ . The scale is clipped at  $1000 S10_{\odot}$  for clarity.

### 3.3. Target Signal

TO DO: Example plots

Next to modelling the background signal, the target signal has to be modelled. Although in reality the radiation emitted or reflected by an asteroid is dependent on a lot of factors, including, but not necessarily limited to, its size, surface composition, shape, temperature and rotational motion, models exist which provide good approximations. As the asteroid population model from **GranvikPopulation** gives a distribution of absolute magnitudes, the starting point of these models will also be the asteroids absolute magnitude, along with the position of the asteroid and the spacecraft relative to the Sun.

Firstly, for determining the emission of an asteroid in the thermal infrared, several models have been constructed in recent years. The original model for asteroids in thermal infrared is provided in the work of **AsteroidSTM**. However, more recently **AsteroidNEATM** have given an updated model of the thermal emissions of asteroids, and therefore their Near-Earth Asteroid Thermal Model (NEATM) is considered the standard at time of writing.

The NEATM assumes asteroids to be spherical, nonrotating body in thermal equilibrium with the radiation emitted by the Sun. The night side of the asteroid is assumed to have a temperature of  $0 \text{ K}$ . The equilibrium temperature is modelled as follows:

$$T(\phi) = \begin{cases} T(0) \cos^{1/4} \phi; & \phi < 90^\circ \\ 0; & \phi \geq 90^\circ \end{cases} \quad (3.10)$$

$$T(0) = [(1 - A)F_{\odot}/(\eta\epsilon\sigma)]^{1/4} \quad (3.11)$$

With  $\phi$  the angular distance from the subsolar point,  $A$  the bond albedo,  $F_\odot$  the incident solar flux,  $\epsilon$  the emissivity,  $\sigma$  the Stefan-Boltzmann constant and  $\eta$  the so-called *beaming parameter*, a correction factor for the emission dependent on the non-sphericalness of the surface, which can be calibrated from observations. For the NEATM, this value is set to  $\eta = 1.22$ .

With the temperature distribution known, the emission can be determined through integration of Planck's law over the visible hemisphere. For this, the size of the asteroid needs to be determined, which can be done using [??](#). Of course, this calculation is sensitive to the assumed value of the albedo. Estimation of this albedo using current data is difficult, however a system utilizing both visual and thermal infrared measurements can use this dependency on albedo to calculate the asteroid's size *and* albedo, instead of only the absolute magnitude.

Calculation of target signal in the visual spectrum is more straightforward, as no integration is needed; a simple phase equation is readily available to obtain the apparent visual magnitude  $V$ , as detailed by **2003NEOSDT**:

$$V = H + 5 \log r\Delta - 2.5 \log [(0.85)\Phi_1 + 0.15\Phi_2] \quad (3.12)$$

$$\Phi_1 = e^{-3.33(\tan \frac{\alpha}{2})^{0.63}} \quad (3.13)$$

$$\Phi_2 = e^{-1.87(\tan \frac{\alpha}{2})^{1.22}} \quad (3.14)$$

For solar elongations less than 60 degrees, **2003NEOSDT** suggest using a modified equation instead:

$$V = H + 5 \log r\Delta + 5.03 - 10.373 \log(\pi - \alpha) \quad (3.15)$$

In these equations,  $H$  is the absolute magnitude,  $\alpha$  is the solar phase angle,  $r$  is the distance from the Sun to the target and  $\Delta$  is the distance from the observer to the target. From the definition of apparent magnitude it follows that:

$$\frac{F_2}{F_1} = 100^{\frac{\Delta V}{5}} \quad (3.16)$$

As the Sun has an apparent magnitude of  $V_\odot = -26.74$ , and a flux of  $F_\odot = 1361 \text{ W m}^{-2}$ , the visual flux can be calculated by:

$$F_t = F_\odot 100^{\frac{-26.74 - V_t}{5}} \quad (3.17)$$

It is here where part of the difficulty of detecting very small NEA's becomes apparent: relative to a  $D = 3.5 \text{ km}$  asteroid ( $V \approx 15$ ), a  $D = 350 \text{ m}$  asteroid ( $V \approx 20$ ) only results in 1/100th of the flux, and a  $D = 35 \text{ m}$  asteroid ( $V \approx 25$ ) will only give off 1/10,000th of the flux in both spectra. Note also that there is no *inherent* advantage to either method in detecting small NEA's when considering the target signal. However, the thermal infrared background signal is relatively lower relative to the target signal (**2003NEOSDT**).

### 3.4. Hardware Properties and Signal-to-Noise Ratio

In addition to the signal properties, the hardware used to image the target is also of interest. Some of the properties of the hardware can then be used to compute the signal-to-noise ratio (SNR) of the target, and some other properties will be used in the next section to determine the search strategy and cadence. **2017NEOSDT** gives a description of representative hardware for current and upcoming space survey telescopes. The overview can be seen in [??](#). For the thermal infrared, a HgCdTe detector is utilized, for the visual light a silicon CCD.

Two important observations should be made from the data in [??](#). Firstly, the visual light system has better specifications with regards to noise and quantum efficiency. This is due to the more advanced level of technology in CCD development compared to thermal infrared detectors. Secondly, the square angle subtended by the visual light sensor is almost five times as large as the thermal infrared sensor, and the required integration time is less than one sixth. The former factor is also due to discrepancies in technological development, the latter is a result of the weaker signal in the thermal infrared band. Together, these factors result in a sizeable decrease in survey cadence, which will be discussed in the next section. A last factor which is not shown in the table is the requirement for thermal infrared telescopes to be cooled to very low temperatures, to avoid the heat of the telescope itself interfering with the measurements. Visual light telescopes are not hindered much by their own temperature, as spacecraft at normal operating temperatures emit very little visible light.

Table 3.1: Representative hardware properties for space-based survey telescopes. (2017NEOSDT)

Parameter	Thermal Infrared	Visual Light
Aperture [m]	0.5	0.5
Field of view [deg]	1.7 x 7.13	10.6 x 5.3
Bandpass [ $\mu\text{m}$ ]	6 - 10	0.4 - 1.0
Integration time [s]	150	24
Quantum efficiency [%]	65	88
Dark current [e-/s]	1	0.00055
Read noise [e-]	22	4

The signal-to-noise ratio of the observation can then be calculated by dividing the signal in  $e^-$  by the root-sum-square of the noise terms, assuming the noise terms to be independent (**DetectionAndTracking**):

$$SNR = \frac{S_t}{\sqrt{S_t + S_b + D + R^2}} \quad (3.18)$$

The target signal  $S_t$  and background signal  $S_b$  can be calculated from the flux  $F$  as follows:

$$S_t = \frac{1}{hc} A \tau k_f Q_e F_t \quad (3.19)$$

$$S_b = \frac{1}{hc} A \tau Q_e F_b \quad (3.20)$$

Here,  $A$  is the telescope aperture,  $\tau$  the integration time of the image,  $k_f$  is the *straddle factor*, a correction factor for the diffraction of a point source ( $k_f \approx 0.9$ ),  $Q_e$  the quantum efficiency, and  $h$  and  $c$  the Planck constant and speed of light, respectively. The noise terms in the SNR equation are:

- $\sqrt{S_t}$ : the poisson noise of the target signal.
- $\sqrt{S_b}$ : the poisson noise of the background signal. Note that the background signal itself can be subtracted fairly easily, and thus only the poisson term has to be considered (see **StarRemoval**).
- $\sqrt{D}$ : the poisson term of the dark current noise. The mean dark current can be removed through proper sensor calibration (see **OpNav**).
- $\sqrt{R}$ : the readout noise.

Thus, the SNR of every target can be calculated at any point in time from any telescope in space in both the thermal infrared and visual light spectrum.

### 3.5. Search Strategy and Cadence

Next, it is important to consider how the telescope will conduct the survey. Of course, a telescope can not view in all directions simultaneously. Very little literature exists on setup and optimization of such search strategies. **Cadence** provides some guidance based on the search strategy for the NEOCam mission. Essentially, the telescope performs a grid-like search, from north to south and west to east. Each section of the sky is revisited four times in a short time to allows for determining the direction of motion of targets, which aids in the precision of orbital determination. Therefore, the survey cadence (the period of imaging the entire sky; i.e. a survey cadence of ten implies the telescope images the entire sky in ten days) can be approximated from the field-of-view and integration time, assuming a slew rate of  $0.5\text{deg s}^{-1}$  and a settle time of 10s as follows for the visual light telescope:

$$T_{survey} = 4 \frac{41253\text{deg}^2}{10.6 * 5.3} * (24 + 10.6/0.5 + 10) = 162134\text{s} \approx 1.88\text{days} \quad (3.21)$$

Which, at a duty cycle of just over 90% represents a fair assumption of the visual survey cadence of 2 days. Similarly, a survey cadence of 21 days was calculated for the thermal infrared system. Note that, as already alluded to in the previous section, the thermal infrared system has a far lower survey cadence, which will hinder the identification performance. Therefore, no system can yet be said to be superior: the thermal infrared system benefits from increased imaging performance, but a worse survey cadence.

### 3.6. Detection and Identification

From the signal-to-noise ratio, detection and identification can finally be established. Firstly, detection of the signal from the noise. As described by [2017NEOSDT](#), detection in processed images is a probabilistic process. At low SNR ( $\text{SNR} < 1$ ), while detection is possible, the detection should be rejected because the probability of false detections becomes too high. Conversely, at high SNR ( $\text{SNR} > 5$ ), detection becomes almost certain. Modelling the process by a normal distribution allows for the intermittent range of SNR to be approximated by an integrated Gaussian. This distribution can be seen in ??.

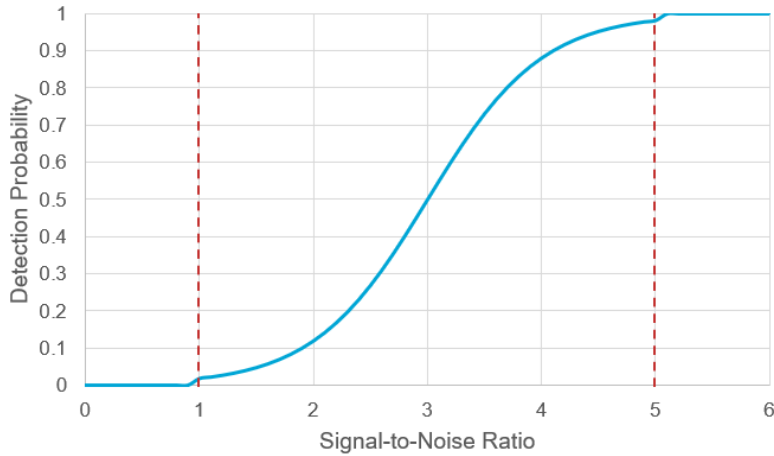


Figure 3.8: Detection probability as a function of signal-to-noise ratio according to an integrated Gaussian. The function is truncated to 0 at  $\text{SNR} < 1$ , and to 1 at  $\text{SNR} > 5$

The process of identification is slightly more complicated. In essence, the process of solving for the orbit of a target asteroid using a single telescope uses Gauss' method, to obtain an orbit from three sets of angular measurements and the time between these. When multiple spacecraft are used and triangulation can be performed, two sets of positions and the time between these is enough to solve for the orbit, per Lambert's problem (see e.g. [Curtis](#) for a thorough treatment of both methods). Theoretically, the time between these observations does not matter much, as long as the period is long enough to ensure that the curvature of the arc is larger than the uncertainty in the measurement ([OpNav](#)). However in practice, the problem of *linking* the observations arises: how does the system know that two observations spaced far apart in time belong to the same object? Currently, in practice, this results in a maximum time of between 30 and 90 days ([DetectionAndTracking](#), [2017NEOSDT](#)). However, it is expected that the resulting maximum will be more towards the maximum due to new techniques such as those presented by [ShortArcs](#) and subsequent papers.

However, these methods rely on data being available throughout the system. It is currently unclear what data would need to be shared precisely, as no multi-spacecraft surveying systems have been researched to that level of detail to date. However, as e.g. [2017NEOSDT](#) state, communication of survey results will be a point of attention for all deep-space surveying missions, not just multi-spacecraft ones, and an advanced communication system along with on-board data processing will be required. Luckily, modern techniques such as machine learning are being used to find computationally unintensive and simple solutions to the image processing pipeline (see e.g. [AIImage](#)). Therefore, this point will be considered to be out of scope of the research presented in this report.

With the detection and identification treated, a full overview has thus been presented of the process from obtaining the signal of both background and target, calculating the resulting SNR, and establishing detection and identification of NEA's. In the next chapter, implementation of these methods will be discussed.

# 4

## Experimental Methodology

After review of the background of near-Earth asteroid surveys and the existing body of literature for modelling surveys, this chapter will discuss the developed simulation in more detail. Firstly, in ??, the architecture of the simulation is discussed on a top-level. Then, in ??, the implementation of the components of the simulation based on the literature in ?? is explained. Then, discourse will be given to the methods of optimization utilized in the research in ?? . Lastly, in ??, the process of using the simulation and optimization methods to obtain the results and conclusions presented in the next chapter is explained as well as the reasoning to support the optimization results. For reference, the interested reader can find the complete code as-is on Github.

### 4.1. Simulation Overview

First, before discussing the specifics of implementation, a general overview of the simulation is given. The objective of the simulation is to accurately predict the performance of a NEA survey by a given system of spacecraft, on a given population. Any optimization or validation is not considered a part of the simulation, but rather a system utilizing it. This will be further explained in ??.

The architecture of the simulation is shown in ?? . On the top left, the main input parameters to the model are displayed. These are primarily the spacecraft and asteroid properties. Both of these consist of a full set of Keplerian orbital elements per spacecraft or asteroid. The asteroid properties furthermore include the albedo, size, and absolute magnitude of each asteroid; the spacecraft properties include which type of payload the spacecraft is carrying.

The simulation consists of a nested loop. Firstly, at the start of each timestep (the time between the timesteps is determined by the survey cadence), the positions of all asteroids and spacecraft are determined by propagation of their orbital elements. Then, in the inside loop, each spacecraft is checked against each asteroid to see if it can detect said asteroid. This is done through calculation of the signal-to-noise ratio (SNR). Lastly, as it is known which asteroids got successfully detected by which spacecraft, it can be determined if asteroids have been identified. Then, at the end of the simulation, the result is a list of the asteroid population in addition to whether they have been detected, and if so, when. Of course, this data can be further processed.

### 4.2. Implementation

In this section, the implementation of the simulation algorithm is discussed. The simulation was written fully in Python 3.8, for reasons of easy testing and iteration, availability of packages for data handling and analysis, and familiarity of the author. The simulations were ran on several computers equipped with consumer-grade 6-core CPU's.

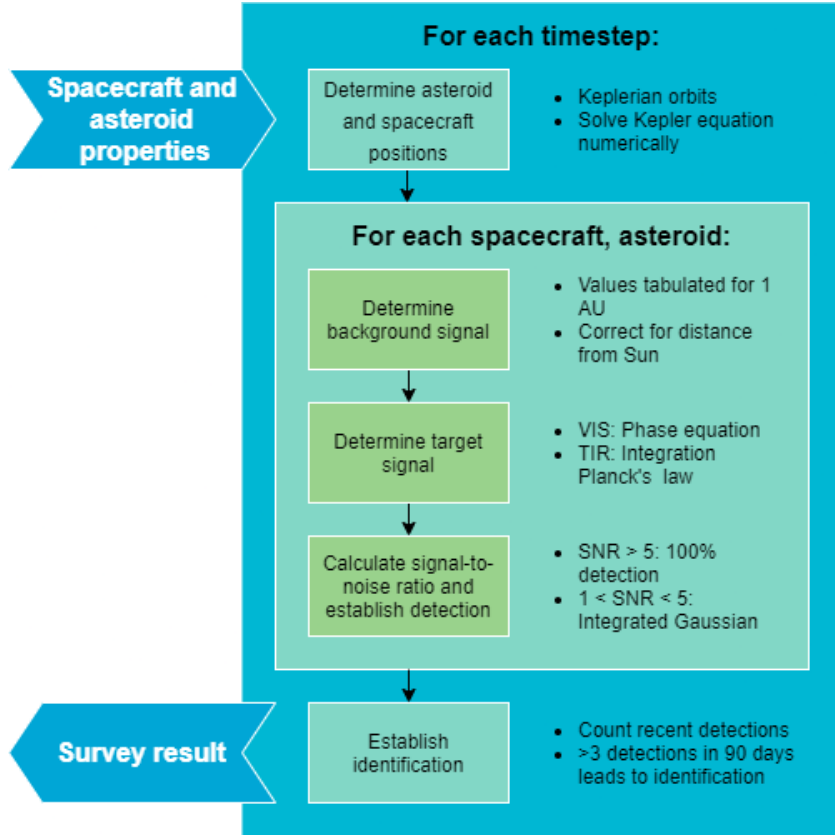


Figure 4.1: Overview of the simulation architecture and main loops.

With regards to specific packages, data handling and computation was performed using Pandas and NumPy. Parallelization was performed using Dask. Critical paths of these packages are written in C/C++/Cython, vastly improving the performance of the simulation. Optimization was implemented through Scikit-optimize and Scikit-learn. Where necessary for the purpose of analysis, data visualisation was performed using Seaborn. Several other packages were used, but their exact functionality and specification is not relevant for the implementation and operation of the simulation.

#### 4.2.1. Population of Asteroids, Spacecraft, and Orbital Mechanics

The population of asteroids was implemented based on the work of **GranvikPopulation**. The authors provide an already generated population model of 802,000 NEA's of absolute magnitude  $17 < H < 25$ . This saves having to implement and validate their modelling separately. For the simulation, a random sample of asteroids is drawn for each simulation run. It was found that a number of 1000 asteroids provided adequate accuracy while reducing computational load. For validation runs, 2500 asteroids were sampled instead to ensure a higher level of accuracy. The model includes for each NEA a unique identifier, a set of six keplerian orbital elements, the absolute magnitude, and the albedo. The data is implemented as a Pandas dataframe. Similarly, the spacecraft are also implemented as a Pandas dataframe, although their orbital elements and payload are given as input arguments to the simulation.

Orbits of asteroids and spacecraft were modelled using Keplerian orbits. As no complex mission geometries or three-body interactions such as impacts are being studied, it was assumed that this would provide an accurate representation. The transcendental Kepler equation was solved numerically using the iterative method proposed by **KeplerEquation**. Resulting orbits and transformations were verified manually. It is noted that calculation of the position of asteroids and spacecraft, especially solving of the Kepler equation, presents one of the largest contributors to the simulation's runtime. For future work, an alternative implementation is recommended.

### 4.2.2. Background Signal

Implementation of the background signal as described in ?? was carried out as follows: Data for visual light is directly provided in the work of **LightOfTheNightSky** in tabulated format for a longitude range of  $[0^\circ, 360^\circ]$ , in intervals of  $10^\circ$ . Latitude coordinates are provided in the interval  $[-90^\circ, 90^\circ]$ , in intervals of  $10^\circ$ . Additionally, latitude values of  $-15^\circ, -5^\circ, -2^\circ, 2^\circ, 5^\circ, 15^\circ$  are provided for additional detail around the brightest areas (such as the galactic core or the Sun). Background signal originating from the Sun uses ecliptic coordinates, signal from the background stars use galactic coordinates. After manual verification, the tables were saved.

The thermal infrared signal as described in **IRDust** was implemented in two steps. Firstly, the thermal infrared background signal from outside the solar system was loaded, and the model for interplanetary dust and sunlight for the Sun-dependent portion of the background signal was implemented. For the latter, the required line-of-sight integration was performed numerically using a Riemann sum with a step size of 0.1 AU, up to a distance of 5.2 AU from the Sun. Results were verified manually by inspection, and comparison of locations of well-known objects in the Milky Way to their locations in the background star signal. The latter step was taken to also ensure that the transformation from ecliptic to galactic coordinates was performed correctly. After verification, the resulting data was tabulated for the same longitude and latitude combinations as the visual light background signal. This was done to ensure universal operation of the code, reducing errors, and to avoid the computational load associated with processing the highly detailed *COBE* data and performing the abovementioned numerical integration.

After tabulation, the background signal data can be held in memory during operation. Where necessary, it can be corrected to account for the spacecraft's distance from the Sun using ???. When necessary, the value of the signal is determined from interpolation by means of Scikit's linear N-dimensional interpolator. ?? and ?? show the resulting background signal in the visual light and thermal infrared, respectively. It can be seen that some loss of detail in the thermal infrared is incurred due to the tabulation, however the effect is minor.

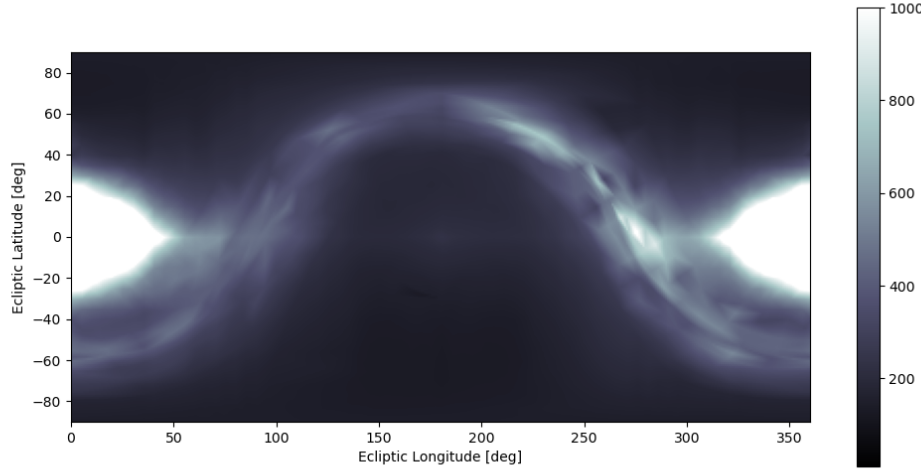


Figure 4.2: Background signal in the visual spectrum, in ecliptic coordinates, as seen from a spacecraft located at  $(-1, 0, 0)$  AU. Units are  $S10_\odot$  or solar-type stars of 10th magnitude per square degree.  $1 S10_\odot = 9.00 \text{ W m}^{-2} \text{ Sr}^{-1}$ . The scale is clipped at 1000  $S10_\odot$  for clarity.

### 4.2.3. Target Signal

Implementation of target signal is a straightforward process. For the visual spectrum, the formulae listed in ?? could be directly copied. The thermal infrared signal involves a triple integration, and is slightly more complex. As this process has to be performed  $n_{\text{asteroids}} * n_{\text{spacecraft}} * T_{\text{simulation}} / \Delta t$  times per simulation, performance has to be taken into account when implementing the integrations.

Firstly, the integration of Planck's law over the bandpass. No closed-form solution exists for the definite

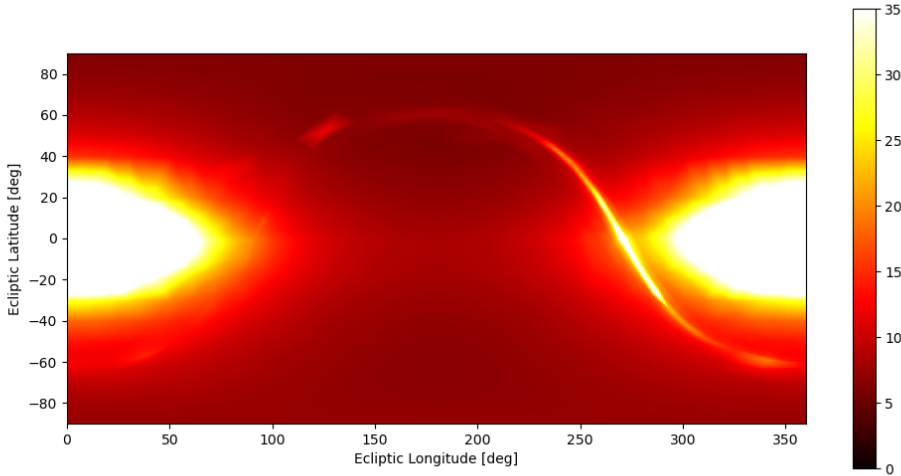


Figure 4.3: Background signal in thermal infrared, in ecliptic coordinates, as seen from a spacecraft located at (-1, 0, 0) AU. Units are Megajansky per steradian,  $1 \text{ MJy sr}^{-1} = 10^{-21} \text{ W m}^{-2} \text{ Hz}^{-1} \text{ Sr}^{-1}$ , and the scale is clipped at  $35 \text{ MJy sr}^{-1}$  for clarity.

integral of Planck's law. As Planck's law is relatively smooth, the decision was made to approximate the integral by the average of the start and end of the bandpass. In practice this means:

$$\int_{6\mu\text{m}}^{10\mu\text{m}} B(\lambda, T) d\lambda \approx \frac{1}{2} [B(6\mu\text{m}, T) + B(10\mu\text{m}, T)] \Delta\lambda \quad (4.1)$$

This essentially approximates Planck's law as a linear function in the domain. It is assumed that this is accurate for the range and temperatures considered. This simplification has to be made, as this integration has to be carried out for every part of the numerical integration over the visible hemisphere of the asteroid, and is thus performed even more often per simulation (in fact, it is the most-called function in the simulation). The integration over the visual hemisphere of the asteroid is performed by first assuming the asteroid to be a sphere. From geometry this integral is well known:

$$F(x) = R^2 \int_{-\pi/2}^{\pi/2} \int_{-\pi/2}^{\pi/2} f(x) \cos\theta \cos\phi d\theta d\phi \quad (4.2)$$

This integration was implemented through a Riemann sum as well, using the midpoint rule and an interval of  $\pi/4$  for both directions, resulting in a total of 16 evaluations. It was found that the error with respect to a very precise integration was less than 1%. Examples of the signal resulting from the implementation can be seen in ?? for the visual wavelengths and ?? for the thermal infrared spectrum.

#### 4.2.4. Search Strategy and Cadence

Implementation of the search strategy and cadence proved to be the most problematic aspect in the implementation process. As mentioned in ??, very little literature exists on the topic, and no methods have been developed to obtain an optimal search strategy utilizing multiple spacecraft. Several options were considered to model the strategy and resulting cadence. Firstly, a method omitting implementation, instead performing a correction ex post, such as utilized by **ThesisOlga**. This method was expected to underrepresent the effect of a distinct survey cadence, and introduces a look-ahead bias which would both be very problematic for the accuracy of the results of this simulation. Secondly, explicitly modelling a north-to-south, west-to-east gridsearch-like strategy such as described by **NEOCam**. Although this model would arguably be the most accurate, it is very impactful with respect to the computational load, for three reasons:

- Firstly, the positions of the asteroids and spacecraft have to be calculated for each imaging step. This results in calculating the positions  $41,253 / (7.13 * 1.7) \approx 3400$  times for thermal infrared, or 734 times for the visual spectrum, for each complete scan of the sky.

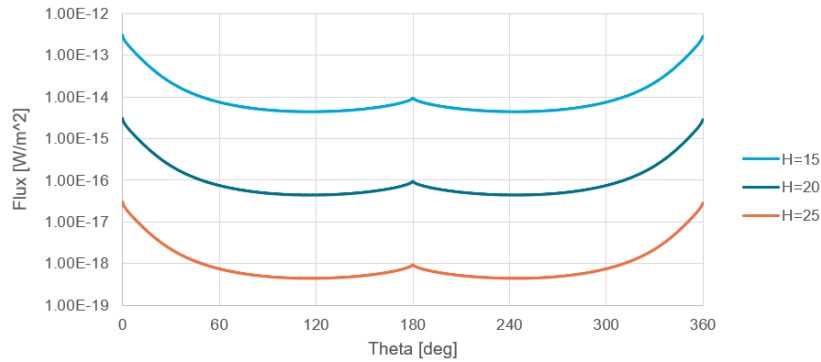


Figure 4.4: Signal in the visual light spectrum of a  $H = 15, 20, 25; p_v = 0.14$  asteroid in a 1 AU circular orbit as seen from a spacecraft at  $(0.7, 0, 0)$ , as a function of the asteroid's true anomaly

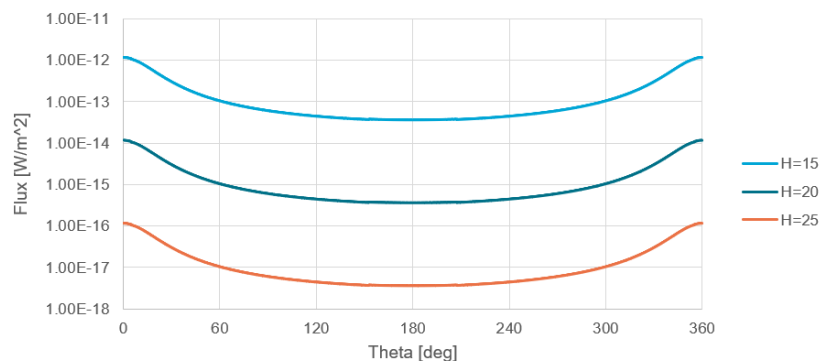


Figure 4.5: Signal in the thermal infrared spectrum of a  $H = 15, 20, 25; p_v = 0.14$  asteroid in a 1 AU circular orbit as seen from a spacecraft at  $(0.7, 0, 0)$ , as a function of the asteroid's true anomaly

- Secondly, to check whether or not an asteroid is inside the field-of-view of the telescope, trigonometric calculations are necessary, which are computationally inefficient.
- Lastly, the conditional logic required to select only asteroids inside the field-of-view prevents parallelization and vectorization of critical parts of the computation.

In addition, as mentioned previously, an optimized multi-spacecraft search strategy would not utilize such a methodology in reality either. Therefore, the claim to increased accuracy is not useful, and not necessarily representative of how the real system would function. The last option considered, which was the one ultimately implemented, is discretization of the entire cadence into a single imaging step, essentially neglecting the search strategy altogether. In practice, this means that instead of modelling out the time per image, the entire timestep of the simulation becomes equal to the cadence, and all asteroids are imaged at the same time once in that interval. For example, for a thermal infrared system with an integration time of 150 s, and a survey cadence of 21 days, this would mean that instead of taking one  $7.13^\circ \times 1.7^\circ$  image every 150 s of a select portion of the sky (one image at  $t=0$ , second image at  $t=150$ s, third image at  $t=300$ s etc.), one “image” is taken of the full sky every 21 days (one image at  $t=0$ , one image at  $t=21$  days, one image at  $t=42$  days, etc.). This might seem to induce a very large discretization error. However, the magnitude of this error is limited:

- An asteroid might move out of the detectable range within the 21 day interval. In this case the assumption causes the asteroid to not be detected. However, conversely, an asteroid might also move into the detectable range in this time period. Assuming both phenomena to be approximately equally common, the error in predicted performance should be small.
- An asteroid might move in the direction of the imaging, causing it to be detected twice in two different fields-of-view, decreasing the time needed to identify the asteroid by providing a second observation within the 21 day window. Again, the converse might also happen with an asteroid being “missed” in this way. Although it might seem this error is therefore also negligible, it is actually not, as most bodies in the Solar system (including NEAs) orbit the Sun counter-clockwise, and therefore a counter-clockwise survey will have slightly more occurrences of double detections than missed detections. Still, considering the relative velocity between the NEA and the spacecraft means that this will also be a rare process.
- Lastly, a quantization error is present due to the maximum window between observations (see ??). Given e.g. a 90-day maximum period between observations, a discretized survey with a 21-day cadence virtually only has a window of 84 days, as the next observation occurs at  $t=105$  days, and is thus outside the 90-day window. It is expected that this will lead to an underestimation of the survey performance, although the influence is also minor, as a repeat observation at  $85 \text{ days} < t < 90 \text{ days}$ , when it was not possible to obtain two follow-up observations prior to this is rare, as the period between close approaches of the NEA and the spacecraft will be in the order of hundreds to thousands of days.

Although the above examples are given for a 21-day thermal infrared survey, it is also of note that the error will be significantly smaller in a visual light system due to the faster cadence. In addition, the error is expected to be roughly equal in magnitude for all simulations, and therefore will have little influence on the optimization process. Considering also the fact that this assumption will provide an estimated 5,000 - 10,000 times faster simulation, this implementation was selected as the best option. The actual effect of the assumption will be validated in REFFF

#### 4.2.5. Signal-to-noise, Detection and Identification

Implementation of the SNR from the target signal, background signal, and hardware properties could be executed directly using the formulae presented in ?? . However, the probabilistic detection model utilizes an integrated Gaussian distribution. As this has no closed-form solution, an approximation based on the hyperbolic tangent function (**GaussianTanh**) was implemented. The function was only applied in the  $1 > \text{SNR} > 5$  range. An  $\text{SNR} < 1$  leads to an automatic failure in detection, and an  $\text{SNR} > 5$  to an automatic success.

For identification, the number and period of the detections are tracked in the asteroid parameters dataframe. For reasons previously outlined, a maximum observation interval of 90 days was assumed. Two criteria can lead to a successful identification:

- Detection on three different timesteps within 90 days by at least one spacecraft. Note that it is not necessary that all three detections are made by the *same* spacecraft.
- Detection on two different timesteps within 90 days, by at least two spacecraft. Again, it is not necessary that these are the same spacecraft. In addition, it is assumed that the triangulation process is always possible: as the sensors have a pixel scale in the order of 1 arcsecond, colinearity is assumed to be a negligible phenomenon.

This means that all communication and image processing requirements are left out of the scope of the simulation. Such requirements, e.g. that the datarate between spacecraft is high enough that they can transmit observations to each other, and that images can be processed on-board, would be design requirements for an eventual mission, such as also already outlined by [2017NEOSDT](#).

### 4.3. Optimization Methods

Before selecting a suitable optimization method, first the optimization problem will have to be formulated. As the objective of the proposed mission is to identify as many unidentified NEAs as possible, the formulation is luckily fairly straightforward: The function is to obtain the highest *survey completeness* possible. The survey completeness is defined as:

$$C = \frac{n_{\text{identified}}}{n_{\text{total}}} \quad (4.3)$$

Or in other words: detect as much asteroids as possible given a set population size. The independent parameters to the optimization will vary throughout the research process, and will be discussed in more detail. The only constraint to be formulated on the problem, is that there is sufficient distance between the spacecraft in the same orbit to allow for accurate triangulation. For simplicity, this was set (arbitrarily) to 0.2 rad, although the behavior of this property will be investigated later.

In order to solve the optimization problem and thus obtain the optimal solutions to the problem, the simulation will be used in conjunction with a mathematical optimizer. A plethora of optimizers exist to date, however a selection of promising optimization methods could be made fairly easily. Firstly, a large number of optimizers, the so-called gradient methods, are reliant on the availability of an analytical solution for the derivative of the function. No way of analytically evaluating the derivative of the simulation was found, and it is expected it does not exist due to the complexity. Therefore these methods can be left out of consideration. A second class of optimizers which is subsequently often considered are the heuristic-based methods, such as particle swarm optimization, simulated annealing, and genetic/evolutionary methods. However, these methods are firstly not guaranteed to find the global optimum, and secondly, require a very large number of function evaluations. Especially the latter is a problem, as the function is a full simulation, which is far from computationally trivial as shown in the previous sections. Therefore, also this class of optimizers can be removed from the selection.

Therefore, it was decided to implement a solution from the class of *surrogate optimization* methods. In these methods, a more simple function is fit to the to-be-optimized function, and it is optimized instead as this allows using a more effective optimizer that can not be used on the function of interest, thereby limiting the number of required evaluations of the main function. The resulting queries to the main function are then used to update the surrogate function. As the surrogate function will eventually very closely resemble the main function, the method is guaranteed to approach the global minimum, provided the function is sufficiently smooth, can be evaluated in the entire domain, and does not have noise (**Surrogate**).

Surrogate functions considered were firstly various machine learning regression methods: Random forest, ExtraRandom Trees and Gradient Boosted Regression Trees, as these methods are capable of fitting to complex functions and do not suffer the overfitting issues encountered by simple decision trees. In addition, Gaussian process regression was tested. Lastly, using an artificial neural network as a surrogate model was considered, but this idea was abandoned as a far larger number of function calls would still be required. As no method exists to determine the ideal surrogate function, this was determined experimentally. It was found that using a Gaussian process as approximation, resulting in the technique of *Bayesian optimization* yielded the best convergence.

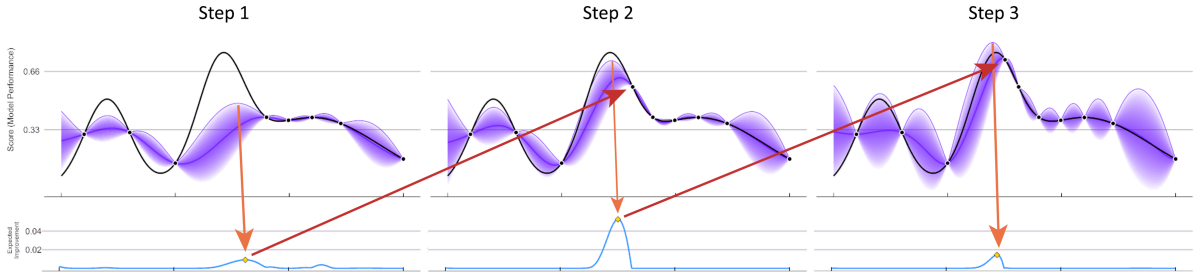


Figure 4.6: Schematic illustration of Bayesian optimization. The to-be-optimized function is shown in black, the Gaussian uncertainty in the purple bands, and the surrogate model is the blue function below. CC BY-SA 4.0 AnotherSamWilson on Wikimedia Commons.

In ??, a schematic representation of the process of Bayesian optimization can be seen. Firstly, a few arbitrary points are sampled on the function. This is done in order to be able to fit a Gaussian probability estimation to the function using the process of kriging. This results in the situation shown in *step 1* in the figure. From the probability estimation, the surrogate model (shown at the bottom) is then determined. The algorithm samples the point which optimizes the surrogate model, and uses it to obtain a new probability estimation, *step 2*. At step 2, the process is repeated, leading to step 3. It can be seen that at this point, the estimation is already close to the global optimum.

In practice this model will be more complex, and therefore requires more evaluations to reach the optimum. This becomes especially apparent as the dimensionality of the problem increases: as the sparseness of the solution space increases, fitting a meaningful Gaussian probability estimate naturally becomes more difficult. A bigger problem, however, is the presence of noise in the function. Due to the random selection of asteroids and the probabilistic nature of the detection model, some noise is to be expected in the results. During the optimization process, care will have to be taken to ensure that the optimizer does not attempt to exploit the noise in the function, as this will lead to an overfit.

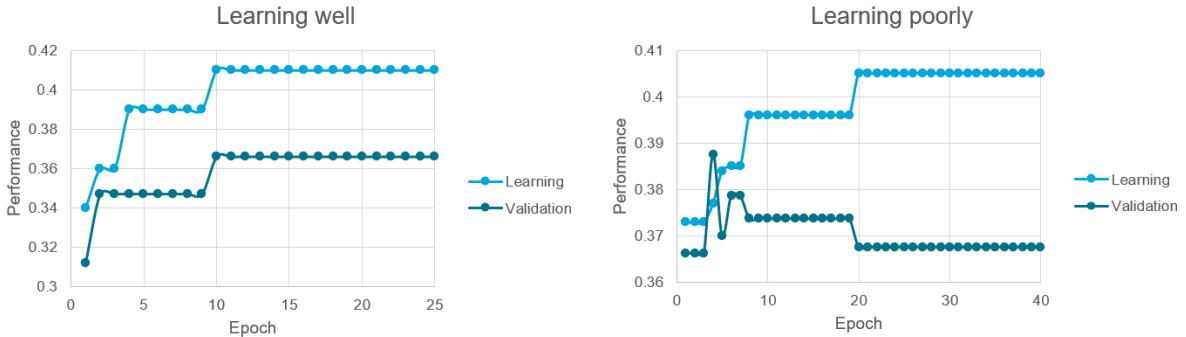


Figure 4.7: Example of a system which learns well, and a system which learns poorly, overfitting instead.

Such *overfit* can be examined by performing a validation calculation at set points during the optimization process. This will provide two sets of survey performance values: the *learning* value, which is the performance predicted by the optimizer, and the *validation* value, which is the performance obtained by evaluating the solution found by the optimizer against an independent dataset. In case the optimizer is learning well, an increase in learning performance will also result in an increase in validation performance. This implies the optimizer has found a feature which is really relevant to the model performance. Alternatively, if the learning performance increases, but the validation performance either stays constant, or even decreases, it means the system is overfitting: the optimizer is attempting to exploit the noise in the signal. An example of this can be seen in ??.

In the case of severe overfitting, such as might occur when a highly dimensional solution is required, a backup method is to use a method based on a random search. This method is extremely simple: throughout the entire solution space, points are uniformly sampled. Then, after a sufficient number of iterations, this process is repeated on a smaller space around the found optimum (this starts a new optimization cycle, essentially “resetting” the overfit), to find a more precise optimum. This can then be repeated a number of times to obtain the global optimum. Although slow and seemingly unelegant, this method has the benefit that it is largely independent of the function itself, and therefore is not prone to overfitting or getting stuck in a local minimum.

## 4.4. Experimental Process

The final consideration in terms of methodology is the actual research process. After implementation of the above, it might be simple to leave the simulation to the optimizer and see what “optimal” solutions results. However, this would not be a prudent course of action. Not only would the survey simulation function as a black box, making it hard to ascertain whether or not the optimizer yields useful results, such an approach would also not provide meaningful insight into the behavior of various parts of the system apart from the optimum itself. Therefore, a more complex research process was set up. The goal of this process is to gain insight into the behavior of individual elements of the solution next to finding the optimal solutions to the problem. Not only will this help in interpreting the results of the optimization, it will also provide a frame of reference for judging the quality of the optimization results to alleviate inherent problems such as noise and overfitting.

The process works up from simple solutions to more complex solutions, evaluating the outcomes at every step. This is mainly related to how much freedom the solution of the system has. However before discussing this, it is important to first establish the position of the number of spacecraft and their payload in this process. With regards to the number of spacecraft, the optimization problem is not very useful: assuming the optimizer functions correctly, an increase in the number of spacecraft will always yield an improvement in the survey completeness, or at worst no change at all. Therefore, as far as survey completeness is concerned, there is logically no *optimal* number of spacecraft. On the contrary, the effect of increasing or decreasing the number of spacecraft in the system is one of the most important goals of the research project. Therefore, the number of spacecraft is treated mostly as a parameter outside of the optimization process, and solutions are tested for a large range of spacecraft. The spacecraft’s payload composition is subject to a similar treatment: although the performance of the systems is dependent on current hardware capabilities, this might change in the future. Therefore, it is interesting to examine the behavior of not only the optimal payload configuration, but also, in more limited fashion, all payload compositions. To complement this, research will be done into the effects of the payload on the performance, and how e.g. hybrid layouts function.

After that distinction, the general research process can be laid out. Firstly, the simulation was extensively verified, as mentioned throughout this section. In addition, where relevant, validation is performed to ensure that results translate to actual applications of the system, and to allow for accurate comparison to other survey proposals. As the validation requires interpretation of the results, it is discussed further after the results, in . Then, as the quality of the simulation has been established, the following research steps are carried out:

1. Through a grid search methodology, all 1-to-1 relations between variables and survey completeness are examined. Although this will not provide very detailed results, it will provide insight into the influence of various parameters. Next to being useful knowledge in and of itself, this will also provide a framework to ascertain the performance of the optimizer later.
2. Using knowledge from the first step, preliminary optimization is carried out to determine a useful range of number of spacecraft for which to carry out more detailed analysis.
3. For this range of number of spacecraft, simple optimizations in which the spacecraft are all in the same orbit (thus limiting the parameter space) is carried out to provide an initial assessment of performance. This process is repeated for different payload compositions to determine the useful payload compositions to continue the analysis with.
4. In parallel, for both visual light and thermal infrared systems, optimization of a system in the same orbit for all spacecraft is performed.

5. Continuing with an optimal range of spacecraft number and payload composition, parameters are increasingly freed up to the optimizer, first allowing for different circular orbits per spacecraft, and later also adding eccentricity. At this stage, a thorough analysis of the optimizer will have to be performed to assess whether the results are valid or the optimizer is starting to overfit.
6. As the complexity increases, the global optimal solutions to the problem are found, and it can be determined how the performance relates to other survey proposals.
7. Lastly, the optimization effort is continued to higher numbers of spacecraft to obtain knowledge on how much asteroids can feasibly be detected. This will round out the research effort by providing a framework for mission designers to base their initial sizing of the system on.

It is expected that the research goals, as formulated in ?? will be adequately answered through this process.

# 5

## Results and Discussion

The research process resulted in numerous interesting findings, with implications both for understanding the behavior of the system, as well as for future design efforts considering multi-spacecraft surveys. These results will be presented and discussed in this chapter. Firstly, the effect of increasing or decreasing the number of spacecraft is discussed in ???. Then, possible payload compositions are assessed in ???. Afterwards, the system's orbital elements, and how these are affected by the composition of the system, will be given discourse in ?? and ?? for spacecraft in identical and differing trajectories, respectively. To aid in the interpretation of these results, a possible explanation for the underlying principle is presented in ???. Finishing the discussion, in ??, predictions will be made with respect to the performance of an optimal multi-spacecraft survey system, and the impact on future design efforts will be discussed.

### 5.1. Number of Spacecraft

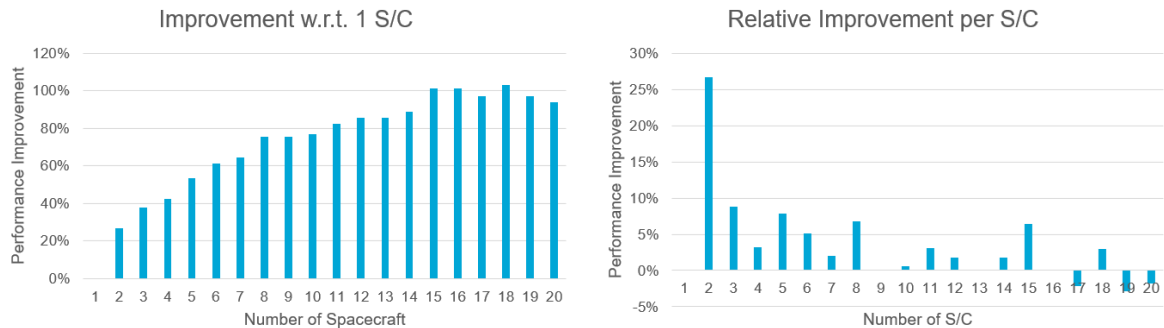


Figure 5.1: Improvement in survey completeness gained by increasing the number of spacecraft in a purely visual light wavelength system. The left graph shows the improvement of an  $n$ -spacecraft system with respect to a system of a single spacecraft, the right graph shows the improvement of an  $n$ -spacecraft system with respect to an  $n - 1$ -spacecraft system.

As explained previously, the number of spacecraft in the system is a parameter that does not have an optimum with respect to the obtained survey completeness: adding additional spacecraft will logically never degrade the performance of the system. However, in practice other constraints (primarily economical) will be present. Therefore, the increase in performance resulting from such an increased investment is of particular interest. ?? and ?? show the performance increase obtained as a function of the number of spacecraft, for the visual spectrum and thermal infrared, respectively. Several observations can be made, which will be listed and subsequently discussed below.

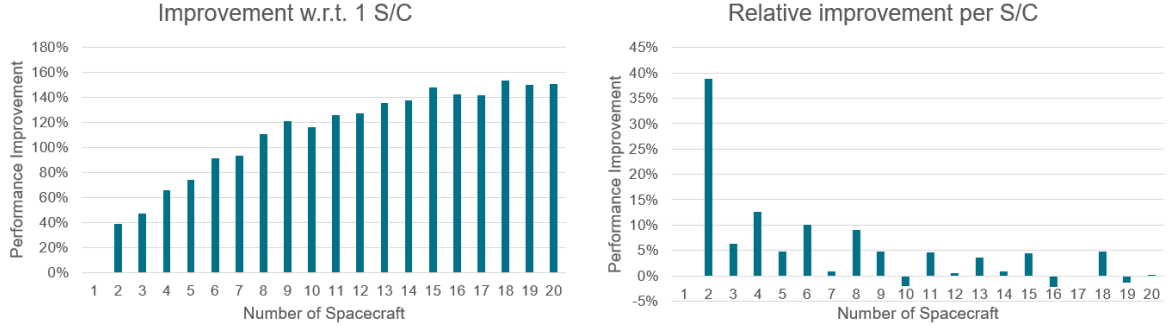


Figure 5.2: Improvement in survey completeness gained by increasing the number of spacecraft in a purely thermal infrared wavelength system. The left graph shows the improvement of an  $n$ -spacecraft system with respect to a system of a single spacecraft, the right graph shows the improvement of an  $n$ -spacecraft system with respect to an  $n - 1$ -spacecraft system.

Firstly, significant diminishing returns present themselves for both spectra; the additional value of an extra spacecraft decreases exponentially with the number of spacecraft already present in the system. Performance increases gained per additional spacecraft fall to around 5% when surpassing 5 spacecraft in the system. Beyond 10 spacecraft, the increases start to fall below the variance in the results, leading to the appearance that addition of spacecraft would yield a decrease in performance, which is logically not the case. This means that, although large initial improvements in performance can be gained from utilizing a multi-spacecraft system, simply increasing the number of survey spacecraft can not bring us arbitrarily close to 100% survey completeness; when increasing beyond approximately 5 spacecraft, it is recommended to focus efforts on improving other areas of the system for the mission to remain efficient.

This fact compounds the second finding: even the most efficient addition - adding a second spacecraft to a single spacecraft survey system - does not come close to increasing the system performance by 100%. In other words: increasing the number of spacecraft will *decrease* the number of asteroids detected *per spacecraft*. While this finding might seem irrelevant from a mission design point-of-view, as the overall performance still increases, it is nevertheless important to consider in the context of other mission constraints, such as budget.

The third result is that thermal infrared systems feature a larger relative improvement to survey performance as the number of spacecraft increases, i.e. thermal infrared systems benefit more from additional spacecraft. This trend continues for higher numbers of spacecraft, with thermal infrared systems reaching a 100% improvement around 7-8 spacecraft, compared to visual light systems requiring 15-16 spacecraft to achieve a similar performance gain. This, combined with the fact that thermal infrared systems have been shown to be the best choice for future NEA missions (see e.g. **2017NEOSDT**, **ThesisOlga**), suggests a multi-spacecraft system should also comprise thermal infrared telescopes. This will be investigated in more detail in ??.

Finally, it is evident that a variance of around 1-2% is present in the survey performance results, relative to a smooth exponentially decreasing curve. It was found that this variance is also present when repeatedly sampling the simulation using the same input parameters. Therfore, in these and subsequent results, it will be assumed that this is simply a result of the stochasticity in the model. Possible other explanations will be ruled out further in REFF.

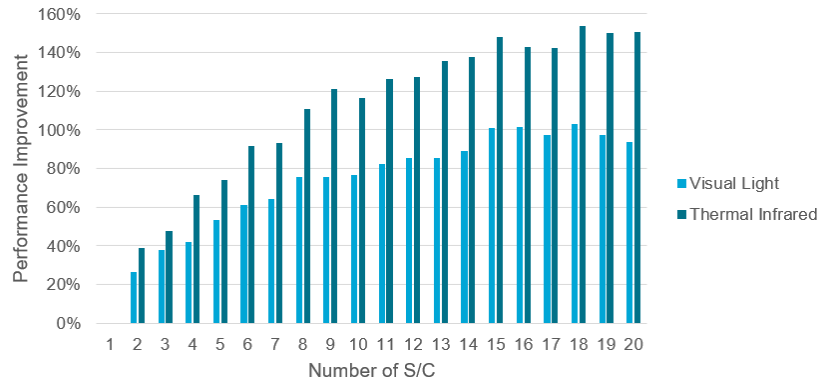


Figure 5.3: Comparison of relative increase in performance gained relative to a single spacecraft system for visual and thermal infrared systems.

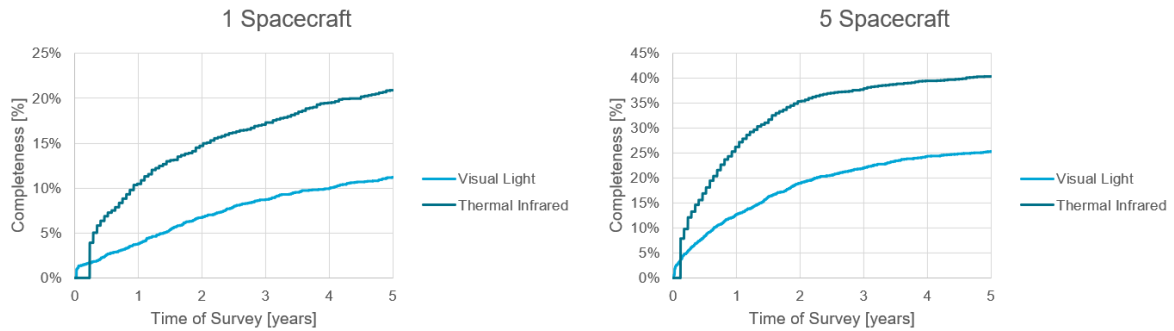


Figure 5.4: Progress of survey completeness over a five year survey for a 1-spacecraft and 5-spacecraft system, comparing visual light and thermal infrared.

## 5.2. Payload

As mentioned in the previous section, initial result suggest thermal infrared systems to be the optimal choice for multi-spacecraft systems because of their predicted higher performance in single-spacecraft systems, and higher benefit from increasing the number of spacecraft. The latter effect is shown in ?? . In this section, the payload composition will be investigated in more detail. Particular interest is placed in the effect of survey length - as visual light systems feature a faster cadence - and in possible synergistic effects in systems featuring both visual light and thermal infrared telescopes. When interpreting the results of this chapter, it is important to keep in mind the fact that these simulations were carried out assuming contemporary hardware. Advances in either type of telescope or sensor might warrant a future reassessment.

Firstly, the performances for systems featuring only one payload type were modelled. For comparison, this analysis was carried out for a 1-spacecraft and a 5-spacecraft system. Because, as shown in the previous section, the payload types exhibit similar behavior when the number of spacecraft is altered, this was assumed to be representative of other numbers of spacecraft as well. The resulting survey performance as a function of time can be seen in ?? . Note that, contrary to previous figures, these graphs show the *absolute* survey completeness, not the completeness relative to a benchmark. In the results, it can be observed that initially, the visual light system features a higher completeness due to its faster cadence. However, the thermal infrared system quickly surpasses it as time progresses. This means that the faster cadence granted by the lower integration times and larger sensor sizes of the visual light system does not weight up to the increased sensitivity of the thermal infrared system on the timescales of survey missions; not only is the final survey completeness more than 10% higher for a thermal infrared system, it also manages to achieve the same performance as a 5-year visual light survey in only a single year in both examined cases. This agrees with the findings of **ThesisOlga** that for systems where quick detections are important, such as impact last-warning, thermal infrared is also a superior option.

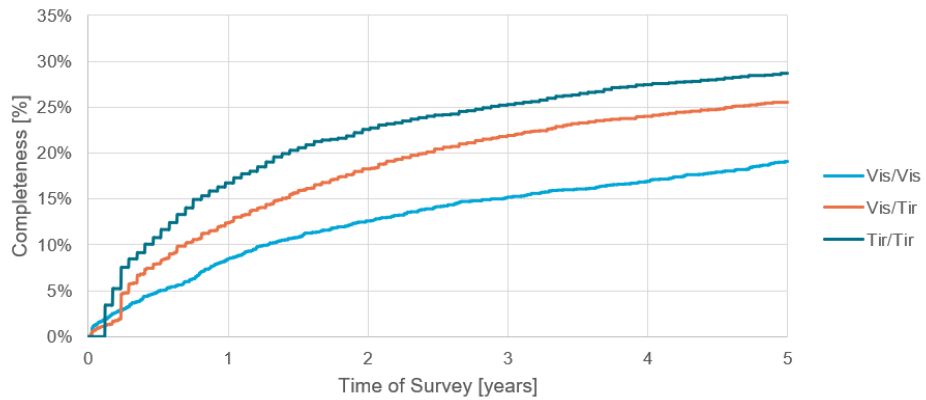


Figure 5.5: Progress of survey completeness over a five year survey for all possible payload combinations in a 2-spacecraft system.

In continuation of the payload analysis, systems utilizing a combination of visual light and thermal infrared telescopes were examined. The reasoning is that the higher sensitivity of thermal infrared systems combined with the higher cadence of visual light systems might result in a synergistic effect where fast, hard to detect NEA's can still be identified successfully. However, as can be seen from the results for 2- and 4-spacecraft systems in ?? and ?? , respectively, this is not the case. A system comprising purely infrared telescopes yields the best results, and performance increases progressively as the number of thermal infrared telescopes in the system increases. This means that in general thermal infrared is the preferred payload type for deep space multi-spacecraft systems. Note however that this assertion is made under the assumption of a "dumb" search strategy, where the system simply repeatedly images the entire sky. Possible applications of fast visual light telescopes as "follow-up" telescopes - as demonstrated by the Catalina Sky Survey - might still be a feasible option, although this would first require research into such advanced search strategies.

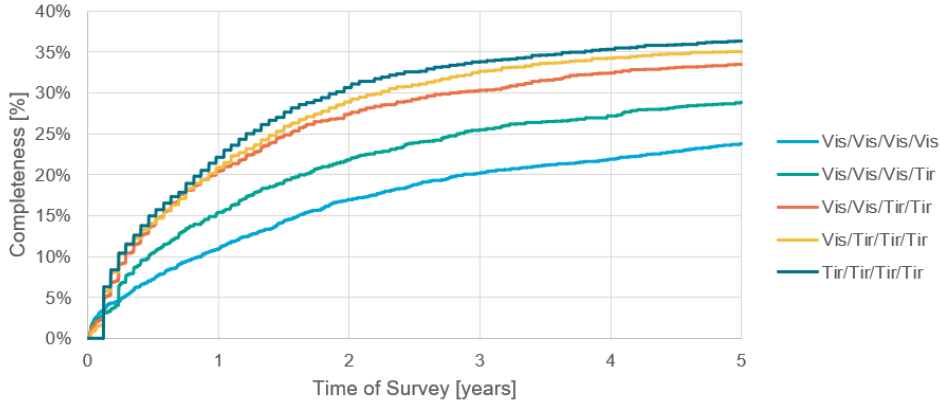


Figure 5.6: Progress of survey completeness over a five year survey for all possible payload combinations in a 4-spacecraft system.

### 5.3. Orbital Elements I: Co-orbital Spacecraft

Next, the orbital elements of the system are inspected. This is done both to find what the effect is of the orbital elements on the performance, but also how the payload and number of spacecraft affect the optimal orbital elements of the system. To facilitate analysis, and to later judge the results of the optimizer more accurately, the orbits are first analysed for a system of co-orbital spacecraft. That is, all orbital elements, except for the anomaly at epoch, are the same for all spacecraft. In addition, the separation in anomalies of the spacecraft is the same for all spacecraft. This was done to vastly reduce the parameter space, and to reduce accidental overfitting to the population model. The latter follows from the fact that, logically, only the angular distance between the spacecraft should influence the result, not the absolute starting position, as the NEAs are distributed in a radially symmetrical fashion. I.e., a system with two spacecraft at mean anomaly at epoch 0 and  $\pi$  should give the same result as starting at  $\pi/2$  and  $3\pi/2$ , only the inter-spacecraft distance is relevant.

#### 5.3.1. Semi-major axis

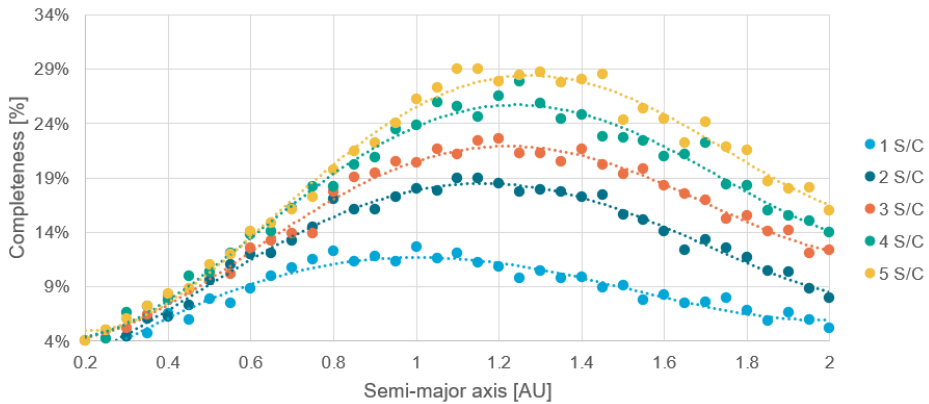


Figure 5.7: Visual light survey performance as a function of semi-major axis for 1 to 5 spacecraft.

In ??, the expected survey performance as a function of semi-major axis is shown for visual light systems, and in ?? for thermal infrared systems. Contrary to the number of spacecraft, it is clear that the semi-major axis has an optimal value. In addition, the region surrounding the optimum is very flat. Thus, locally, the solution is not sensitive to changes in semi-major axis up to a distance of approximately 0.1 AU from the optimum. Two important conclusions are drawn here: Firstly, a wide range of semi-major axes lead to a well performing system. Secondly, due to the variance in results discussed earlier, it is difficult to pinpoint an exact optimal value. Therefore, in mission design, other considerations can and should be prioritized to determine a more precise semi-major axis.

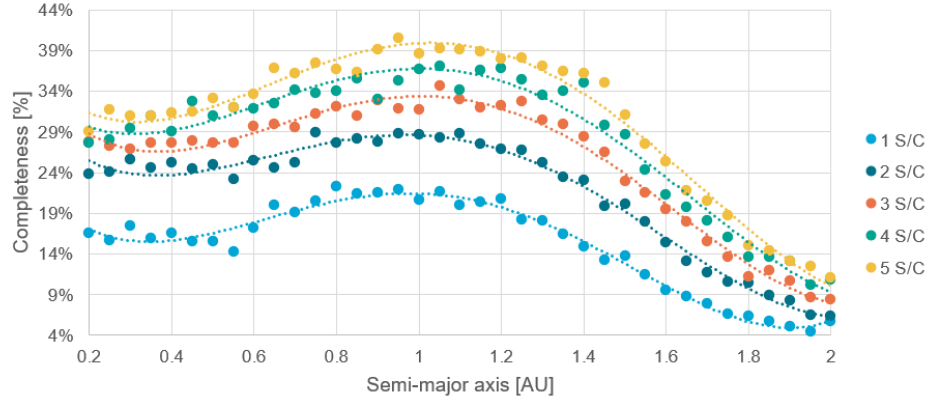


Figure 5.8: Thermal infrared survey performance as a function of semi-major axis for 1 to 5 spacecraft.

The second factor of note is the change in the optimal semi-major axis as the number of spacecraft increases. It can be observed that for visual light systems, the optimal semi-major axis is essentially unchanging for  $n \leq 5$ . However, for thermal infrared systems, there is clearly an increase in optimal semi-major axis as  $n$  increases. This is further illustrated in ??, where the optimal semi-major axis is given as a function of the number of spacecraft explicitly. Here, it can be observed that the optimizer indeed has difficulty pinpointing the exact optimum, but instead finishes on a value somewhere in the optimal range. In addition, the semi-major axis becomes larger for higher numbers of spacecraft for thermal infrared systems. For visual light systems at higher numbers of spacecraft this also starts to occur. An explanation for this phenomenon is proposed in ??.

TO DO: Getallen noemen.

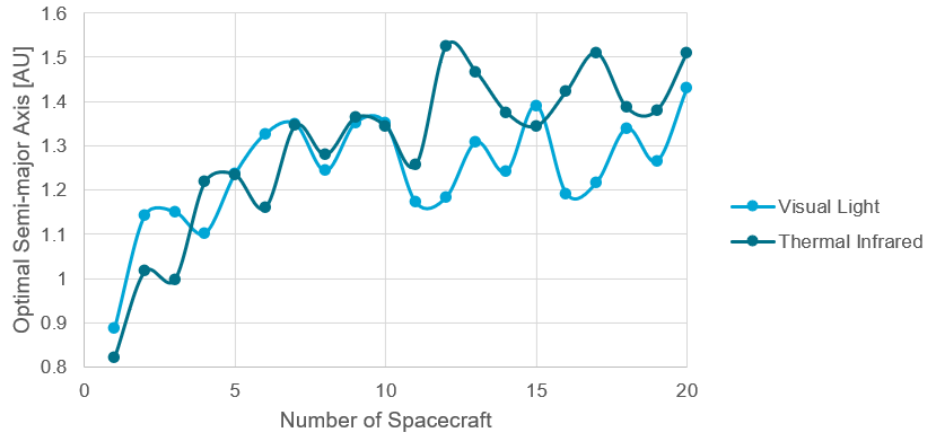


Figure 5.9: Optimal semi-major axis as a function of the number of spacecraft in the system.

### 5.3.2. Eccentricity

Results with regards to varying the eccentricity are shown in ?? for visual light systems and ?? for thermal infrared systems. It is readily apparent that for both systems, a circular orbit is preferred. It is hypothesized that this is the case because eccentricity causes the system to deviate from the optimal semi-major axis found in the previous subsection. This is further supported by the empirical finding that the optimal semi-major axis at a given eccentricity results in an apohelion distance roughly equal to the optimal semi-major axis at 0 eccentricity. That is:

$$a_{opt}(e) \approx \frac{a_{opt}(0)}{1+e} \quad (5.1)$$

This is further illustrated in ?? . This result is theorized to occur because the spacecraft will, in this solution, still spend a large portion of its orbit in the optimal semi-major axis range. However, not enough data are available to ascertain statistical significance for this finding.

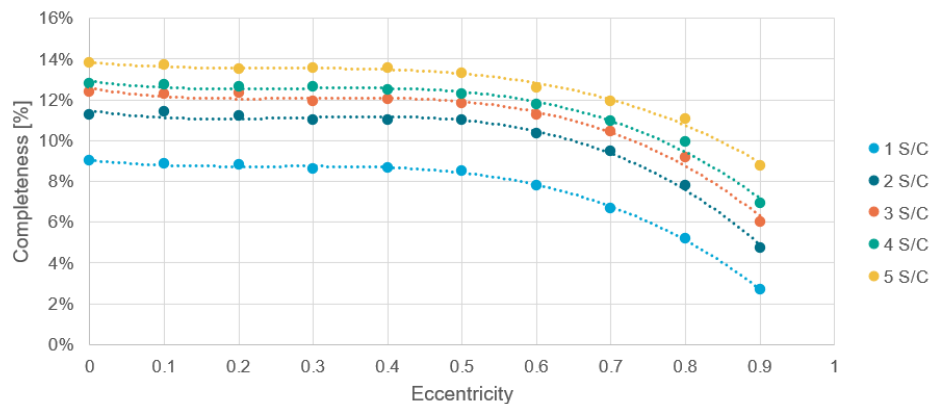


Figure 5.10: Visual light survey performance as a function of eccentricity for 1 to 5 spacecraft.

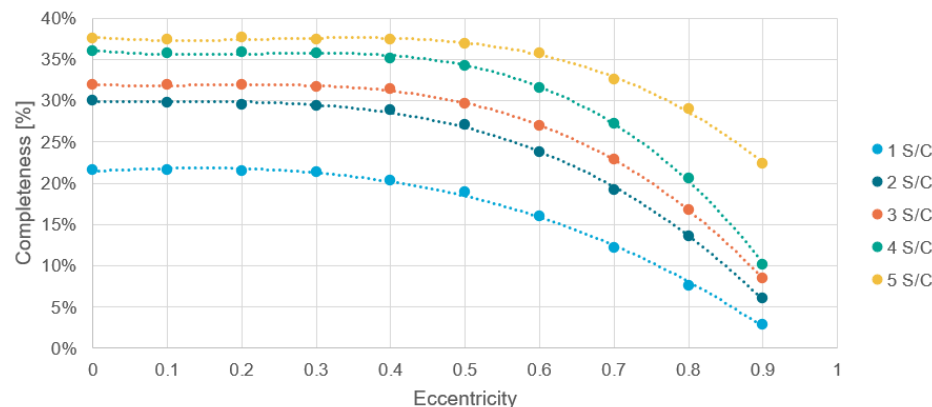


Figure 5.11: Thermal infrared survey performance as a function of eccentricity for 1 to 5 spacecraft.

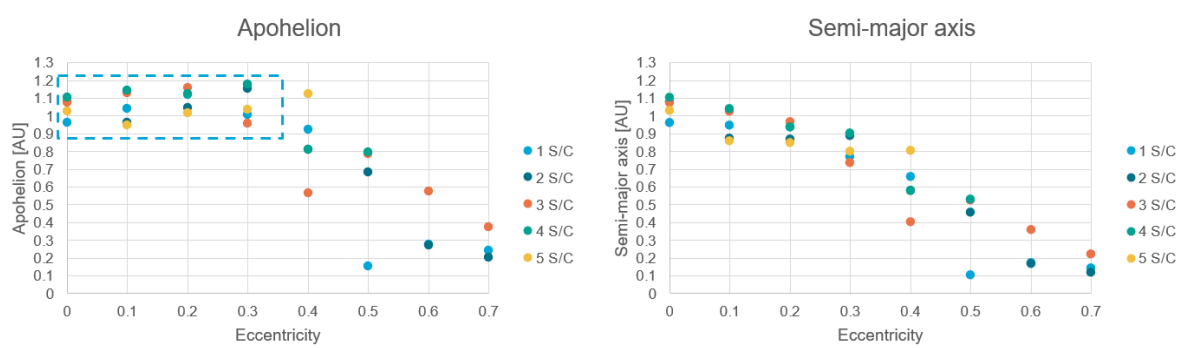


Figure 5.12: Relationship between optimal semi-major axis, eccentricity, and the resulting perihelion for 1-5 spacecraft.

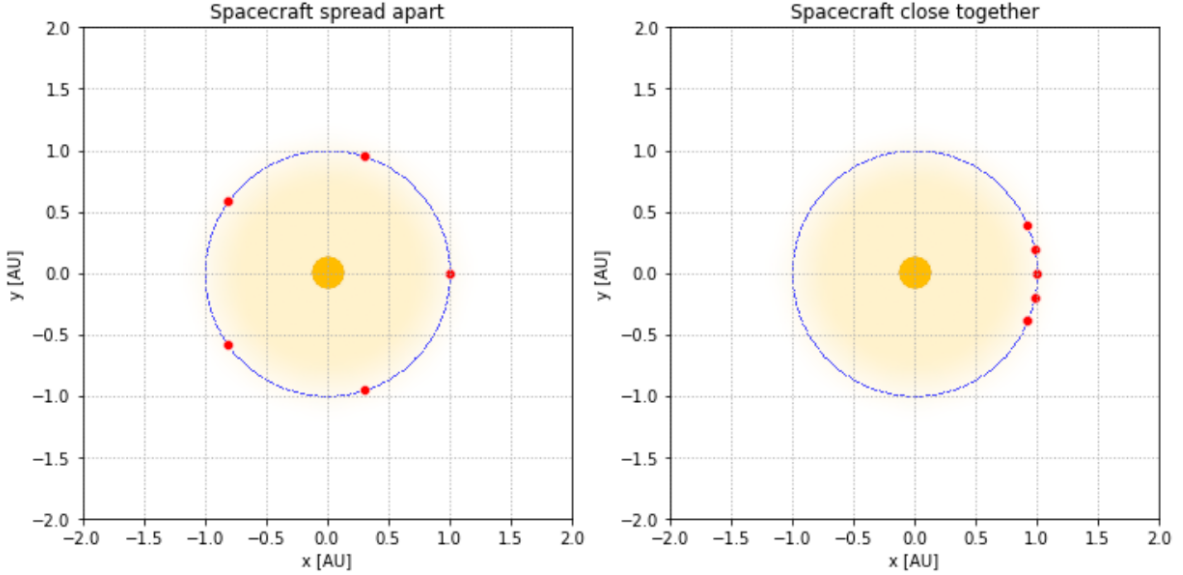


Figure 5.13: Illustration of a high ( $2\pi/5$  rad) and a low (0.3 rad) inter-spacecraft distance.

### 5.3.3. Mean Anomaly at Epoch

The last parameter to be considered for the co-orbital solutions is the mean anomaly at epoch. As previously explained, the mean anomaly will not be considered for each spacecraft separately. Instead, the concept of inter-spacecraft spread is introduced. This inter-spacecraft spread is simply defined as the difference in anomaly at epoch of one spacecraft to the next, in such a way that the formation is centered around  $\theta = 0$ . This means that, with inter-spacecraft spread  $\Delta\theta$ , the mean anomaly at epoch  $\theta$  of spacecraft  $n$  in a system of  $N$  spacecraft is:

$$\theta_n = (n-1) \cdot \Delta\theta - \frac{N-1}{2} \Delta\theta \quad (5.2)$$

This equation and the resulting formation is shown in ???. A lower boundary of 0.3 rad was chosen to ensure triangulation would remain possible. In addition, to maintain the separation between all spacecraft, the full formation can not span more than  $2\pi$  rad. This results in the boundaries  $0.3 \leq \Delta\theta \leq 2\pi/N$ . The hypothesized effect of changing the spread is composed of two effects: On the one hand, spreading out the spacecraft more allows for viewing a larger portion of the sky simultaneously, and reduces blind spots, as explained in REFFF. On the other hand, as spacecraft are closer together, the chances of obtaining a simultaneous detection of the same asteroid - and thereby achieving triangulation - is increased, thereby leading to a faster detection.

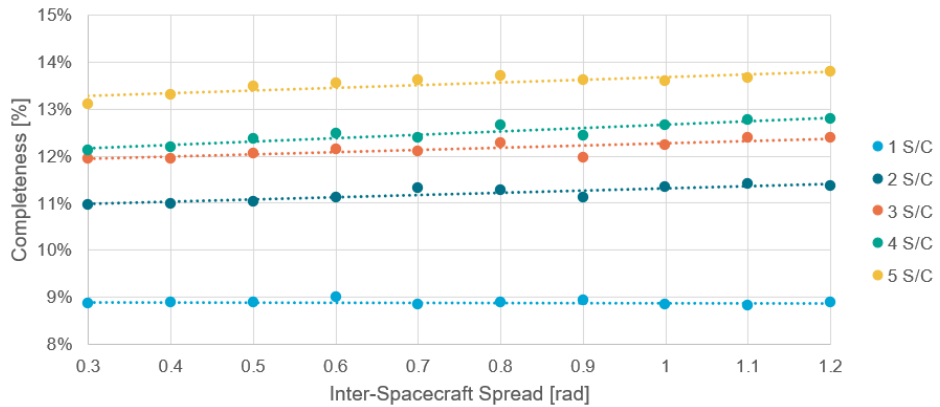


Figure 5.14: Visual light survey performance as a function of angular separation between spacecraft for 1 to 5 spacecraft.

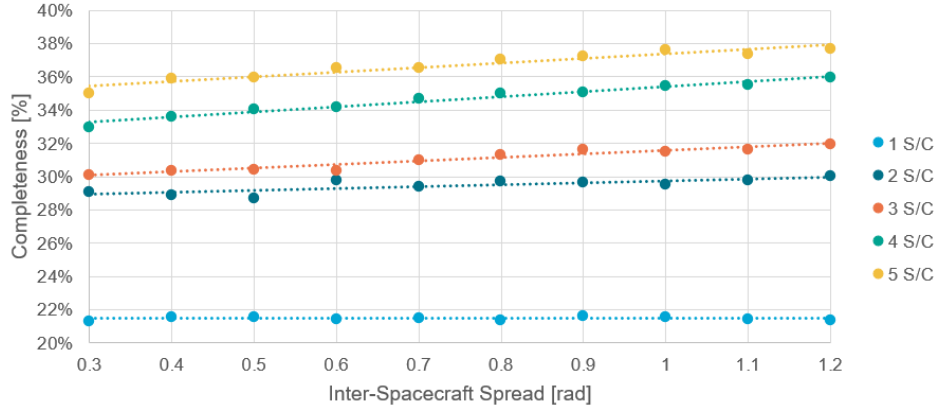


Figure 5.15: Thermal infrared survey performance as a function of angular separation between spacecraft for 1 to 5 spacecraft.

Results for visual light and thermal infrared are shown in ?? and ??, respectively. It is observed that an increase in the angular distance between the spacecraft will increase the performance of the system. Therefore, the effect of observing a larger part of the sky effectively is stronger than the increased chance at successful triangulation. Practically, this implies that a multi-spacecraft survey should aim to distribute the spacecraft as much as possible over the orbit, even if e.g. communications requirements do not allow the system to be spread out over the entire orbit.

## 5.4. Orbital Elements II: Non Co-orbital Spacecraft

A logical continuation of the above analysis would be to investigate systems in which all spacecraft are allowed to have different orbital elements per spacecraft. This complicates the analysis significantly, as the dimensionality of the problem rapidly increases. Therefore, additional special attention has to be paid to the performance of the optimizer, and to run validation tests on its results. In addition, to aid in comparison, three sets of optimization parameters were analysed. Firstly, a system which has all spacecraft spread out as much as possible, in a single circular orbit. From the results in the previous section, it follows that this is the optimal solution. Secondly, a system in which each spacecraft can have a distinct semi-major axis and anomaly at epoch. Because spacecraft with different semi-major axes have different orbital periods, the spacecraft can not be spread out evenly a priori. Therefore, the optimizer has to take care of this task as well, and not just the semi-major axes. Lastly, a similar set of parameters is analysed, but with orbits that are allowed to be non-circular. In that case, the parameter space comprises a semi-major axis, true anomaly at epoch, and eccentricity for each spacecraft.

The results of the optimization processes can be seen in ???. It can be seen that several performance breakpoints are present: for low numbers of spacecraft, approximately  $1 \leq n \leq 5$ , all three methods result in similar performances. Then, for approximately  $6 \leq n \leq 10$ , the performance of the optimization including eccentricity starts degrading relative to the other two. Lastly, for  $n > 10$ , the “simple” solution with the spacecraft in the same orbit, spaced equally, is superior to the other two methods. These results might be surprising to some readers: one would expect the performance to either increase, or stay equal, as more parameters become available to the optimizer. After all, all solutions found for a circular, co-orbital system of spacecraft (i.e. only a single semi-major axis gets determined by the optimizer), can be recreated by the other two optimizers, and therefore they can reach the same performance. The source of this discrepancy is twofold. The first aspect is the problem of the optimizer overfitting to the noise in the system. The second aspect is related to the actual performance benefits obtainable through these more complex solutions. Although the results here might seem inconclusive, the combination of both aspects will allow drawing some important conclusions.

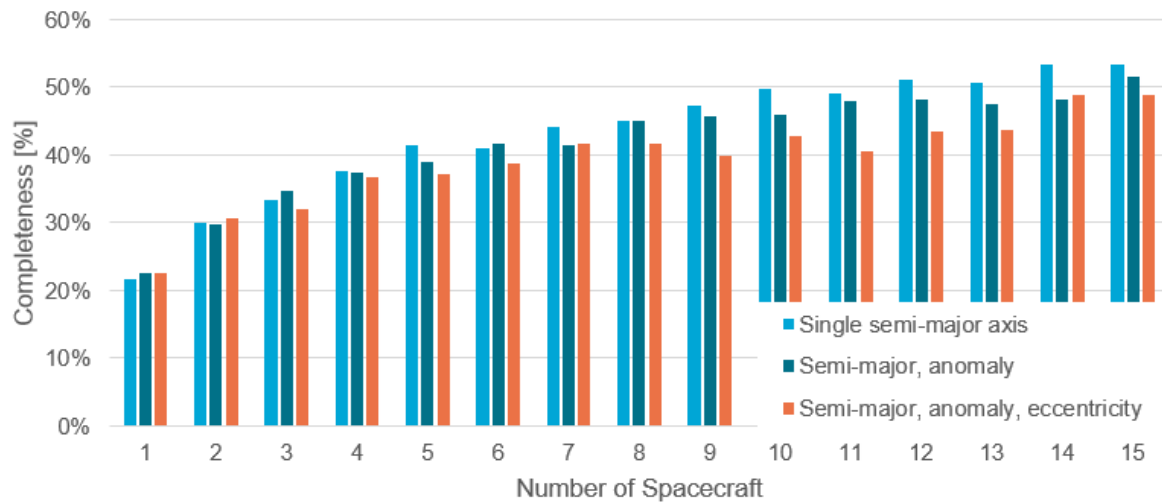


Figure 5.16: Performances for systems optimized for either a single semi-major axis, distinct semi-major axes and anomalies per spacecraft, or distinct semi-major axes, anomalies and eccentricities per spacecraft.

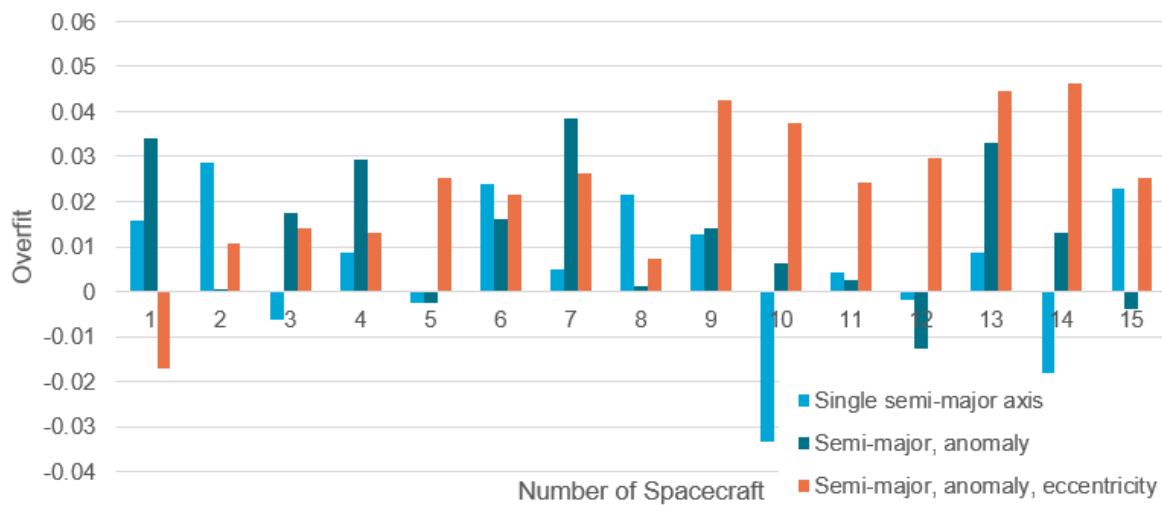


Figure 5.17: Overfit of the optimizer per number of spacecraft.

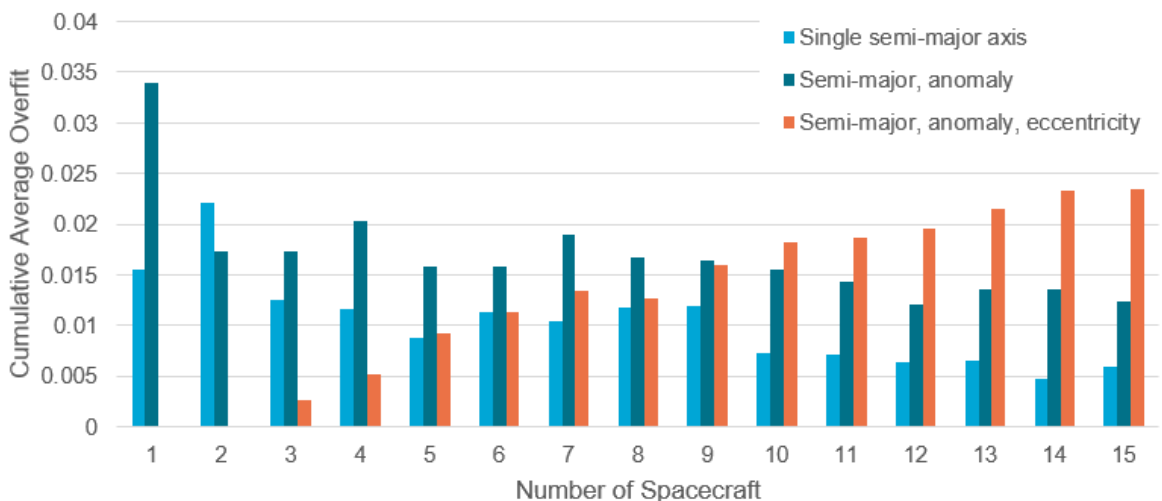


Figure 5.18: Cumulative average of the overfit of the optimizer per number of spacecraft.

First, the problem of overfit will be addressed. To illustrate the occurrence of overfit at higher dimensionalities, ?? gives the overfit for each optimization problem, per spacecraft. Overfit is defined simply as the difference between the learning performance (i.e. the performance predicted by the optimizer for its solution) and the validation performance (the actual performance which can be expected at the solution). As ?? is hard to interpret directly, ?? provides the cumulative average up to and including a certain number of spacecraft. Several observations are made here:

- As the number of spacecraft increases, the average overfit of the single semi-major axis system decreases. In other words, for a higher number of spacecraft, the optimizer performs better. This occurs because, in this system, the dimensionality does not increase, and therefore the task of the optimizer is equally hard. However, as the distribution of spacecraft becomes more uniform, the system will overfit less to the population as the importance of the starting position of each spacecraft becomes smaller. In other words, a higher number of spacecraft incurs a regularizing effect on the optimizer.
- Secondly, the average overfit for the system with distinct semi-major axis and anomaly, but no eccentricity, per spacecraft, exhibits no statistically significant slope. The degree overfit levels out around 1-1.5%. At this degree of overfitting, the optimizer is capable of finding a solution to the problem.
- Lastly, the system optimized for semi-major axis, anomaly and eccentricity, shows an *increase* in overfitting. I.e., the optimizer is not capable of keeping up with the increasing dimensionality of the problem, and the quality of the result continually decreases.

Before investigating the second point, first some of the solutions of the optimizer will be examined, along with their training progress. The solutions to be investigated are two, six and eleven spacecraft. The one spacecraft case is omitted as the optimal solution is already known from previous analysis to be the optimal solution to the single semi-major axis system. The six and eleven spacecraft cases were chosen as they represent the first solution after the performance breakpoints discussed earlier.

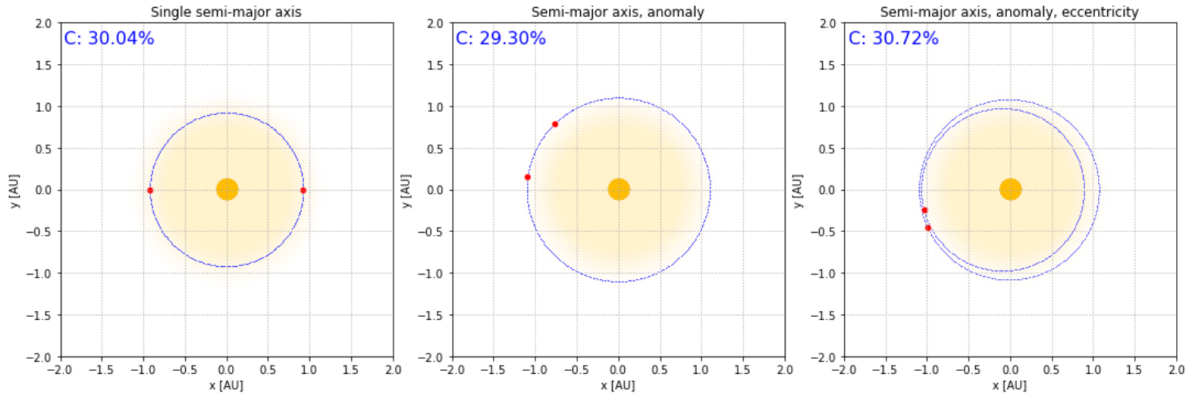


Figure 5.19: Optimization results for systems with two spacecraft.

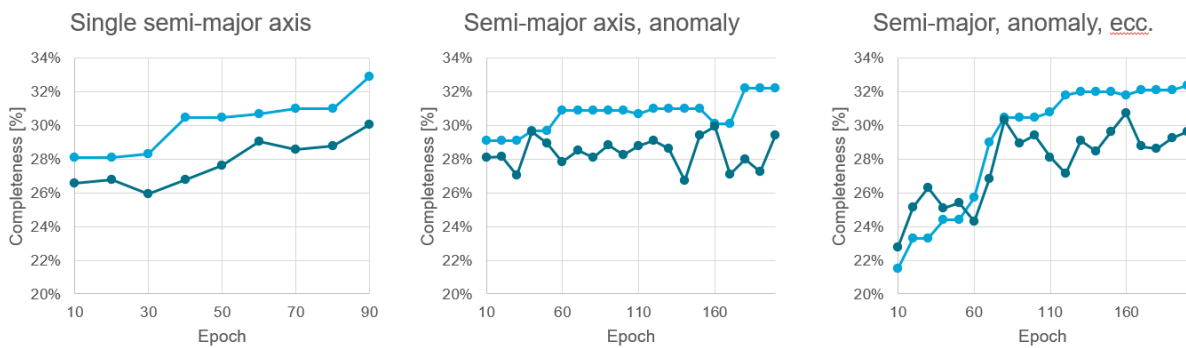


Figure 5.20: Learning/validation results for systems with two spacecraft.

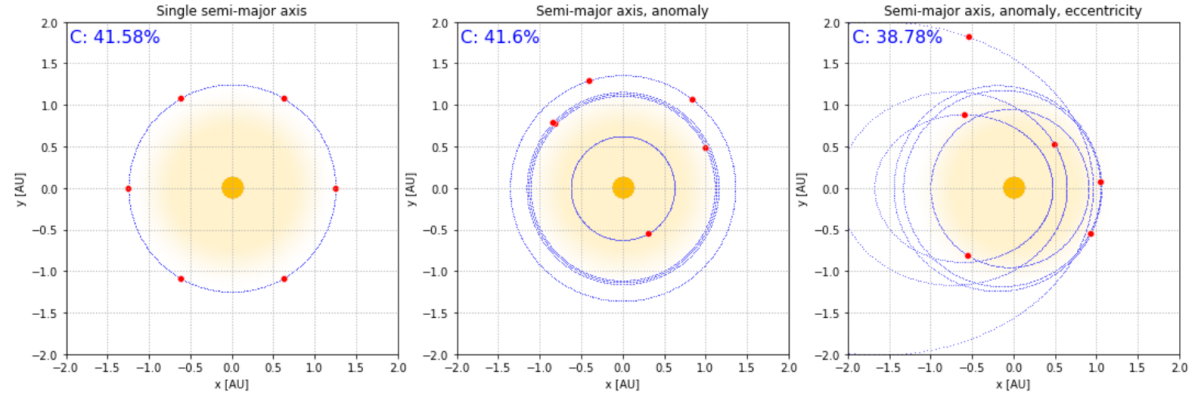


Figure 5.21: Optimization results for systems with six spacecraft.

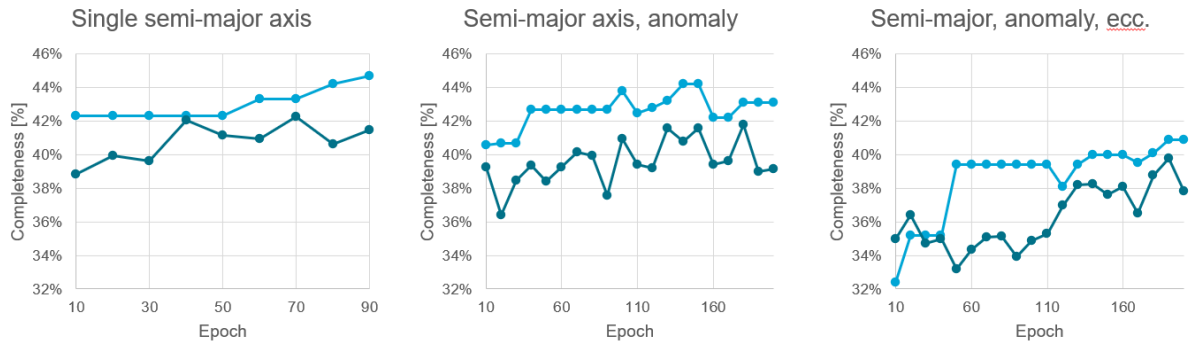


Figure 5.22: Learning/validation results for systems with six spacecraft.

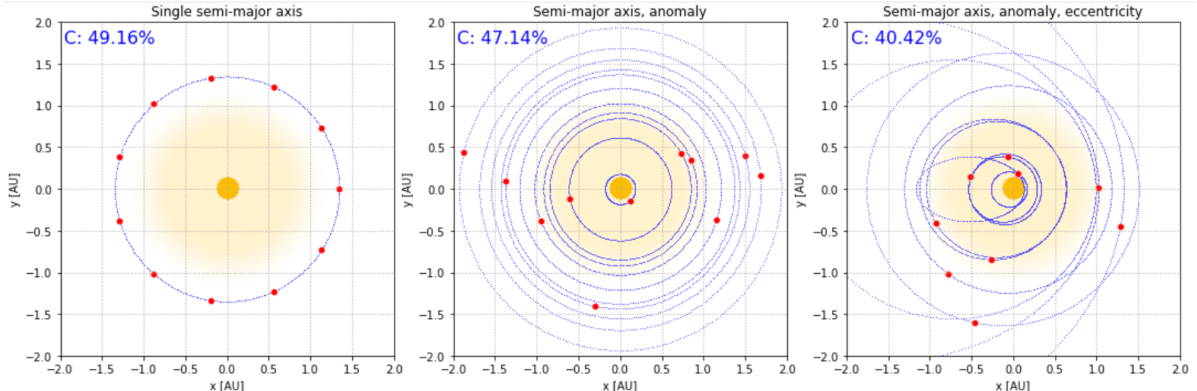


Figure 5.23: Optimization results for systems with eleven spacecraft.

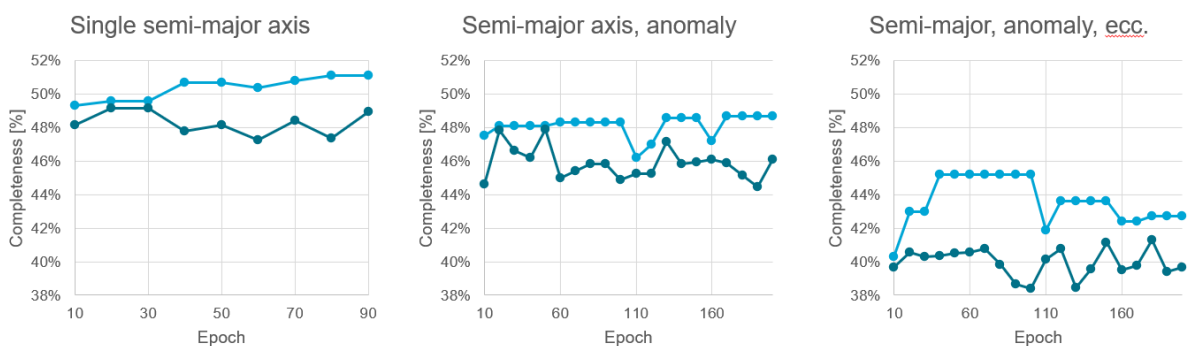


Figure 5.24: Learning/validation results for systems with eleven spacecraft.

## 5.5. Explanation of Observed Phenomena

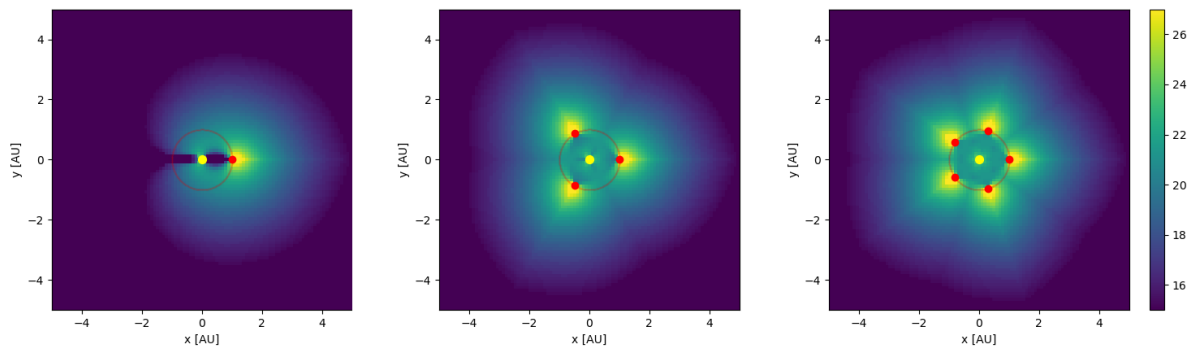


Figure 5.25: Illustration of the observable area for a system of 1, 3 and 5 spacecraft, spread out over the orbit.

## 5.6. Predicted Performance and Implications for Missions Design

20%: 1 30%: 2 40%: 6 50%: 15 60%: 50 70%: 200

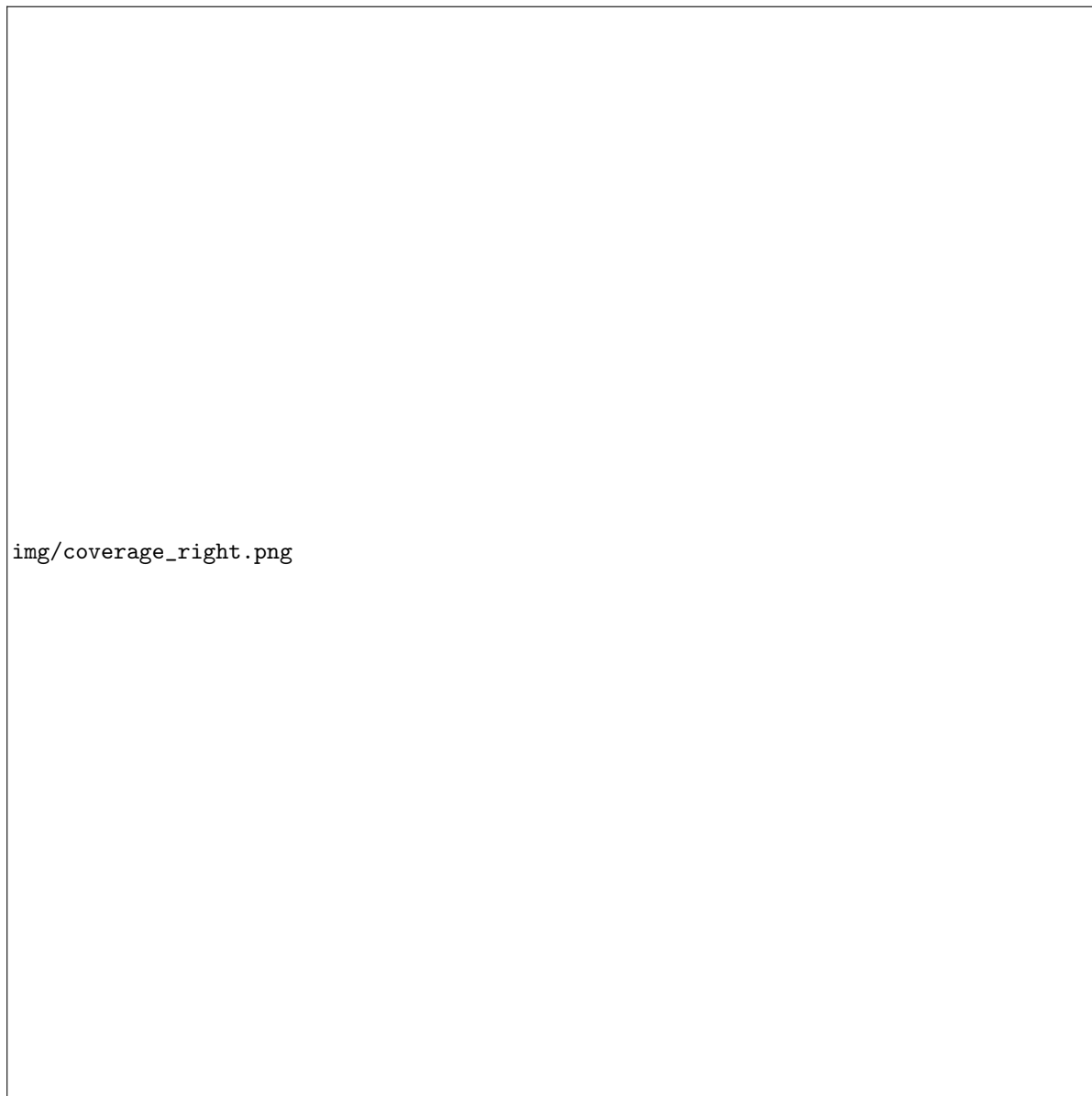


Figure 5.26: Illustration of the observable area for a system of 1, 3 and 5 spacecraft, spread apart by 0.2 rad.

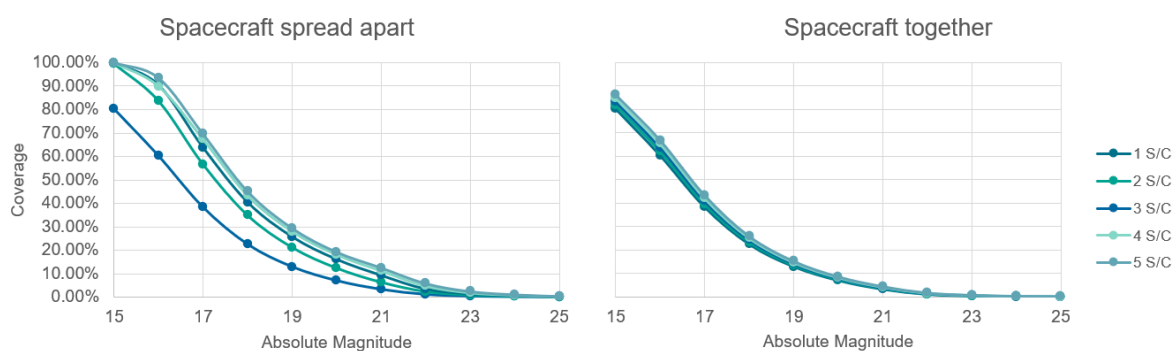


Figure 5.27: Relationship between coverage and asteroid absolute magnitude for spacecraft spread maximally apart, or spread only 0.2 rad

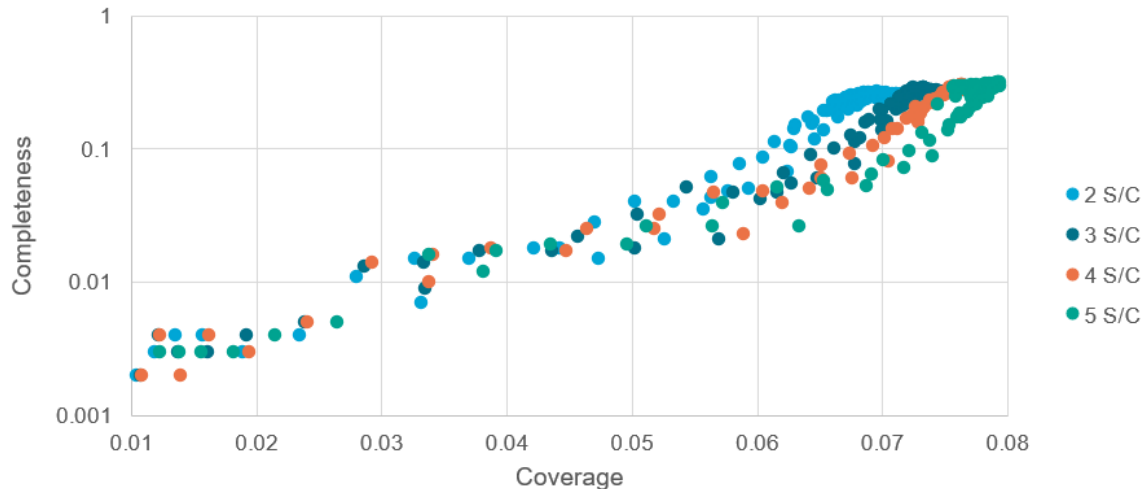


Figure 5.28: Relationship between coverage and completeness for 2-5 spacecraft.

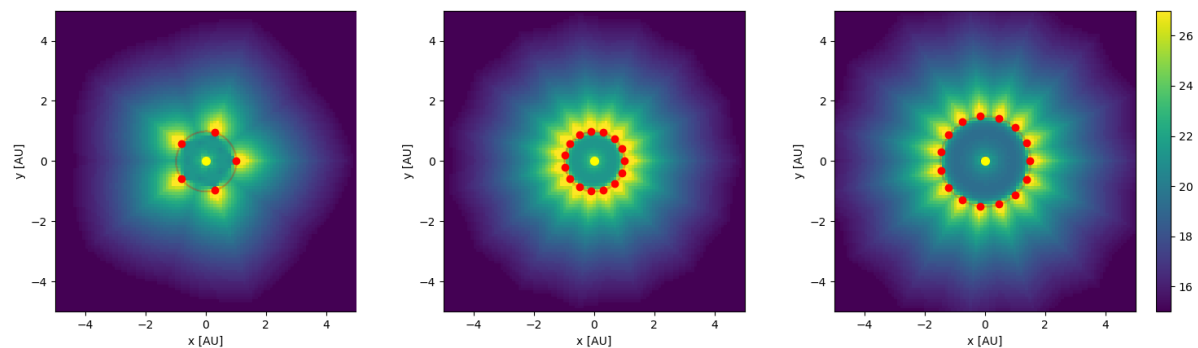


Figure 5.29: Illustration of the observable area for a system of 15 spacecraft, at  $a=1.0$  AU and  $a=1.5$  AU, spread out over the orbit. The 5 spacecraft case is shown for comparison.

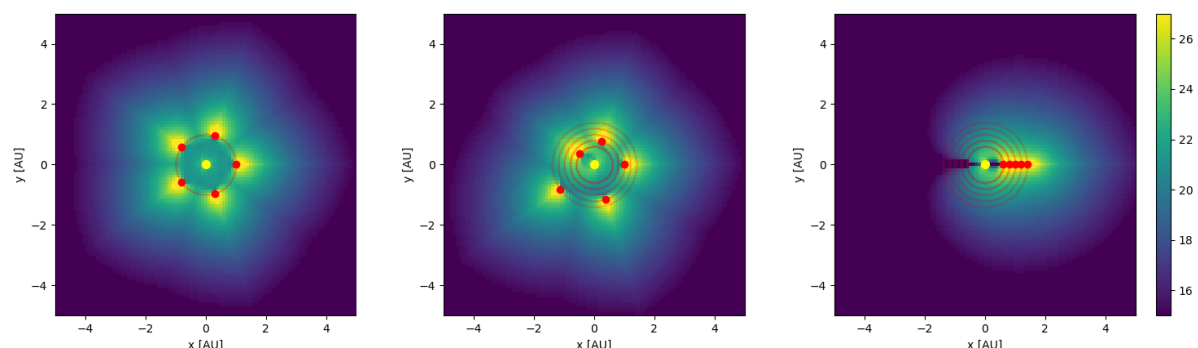


Figure 5.30: Illustration of the observable area for a system of 5 spacecraft, spread out over the orbit. The left case has the spacecraft co-orbital. In the middle case, the spacecraft are in different orbits, but spread out. On the right, they have lined up in their orbital motion.

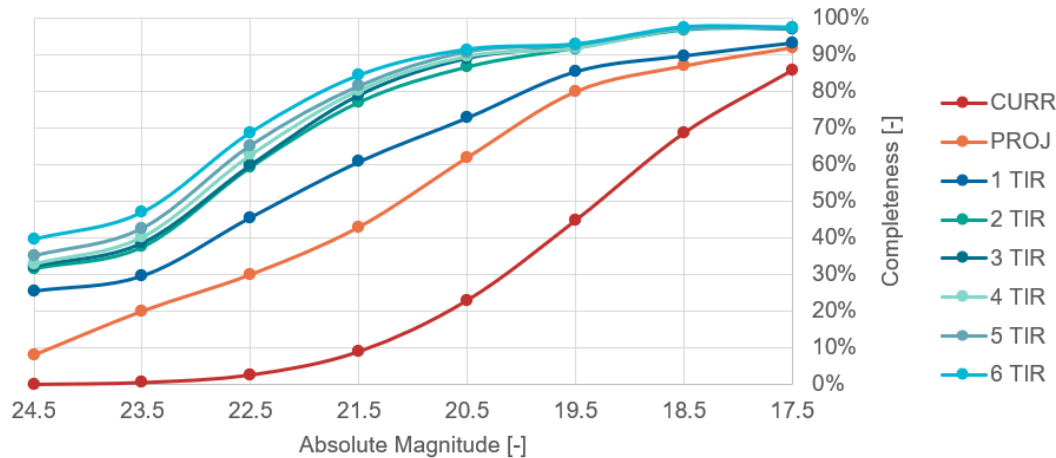


Figure 5.31: Prediction of performance

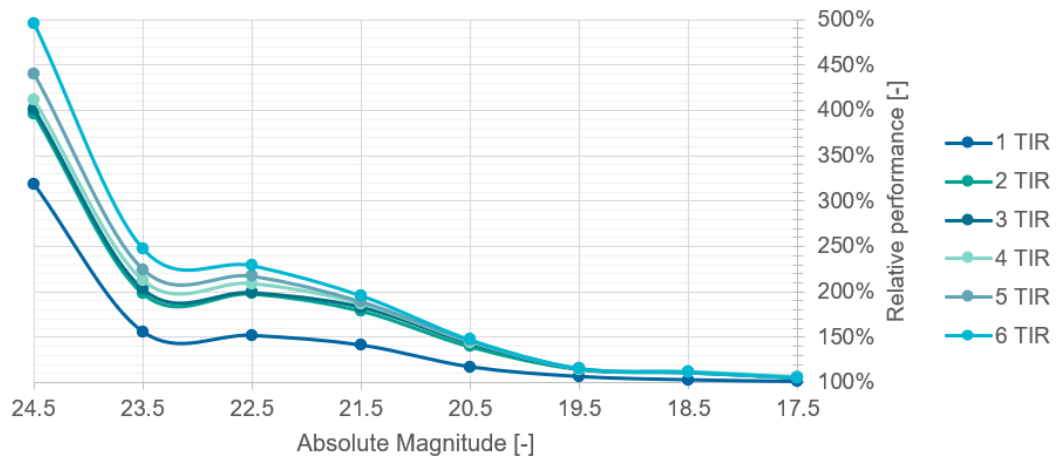


Figure 5.32: Relative prediction of performance

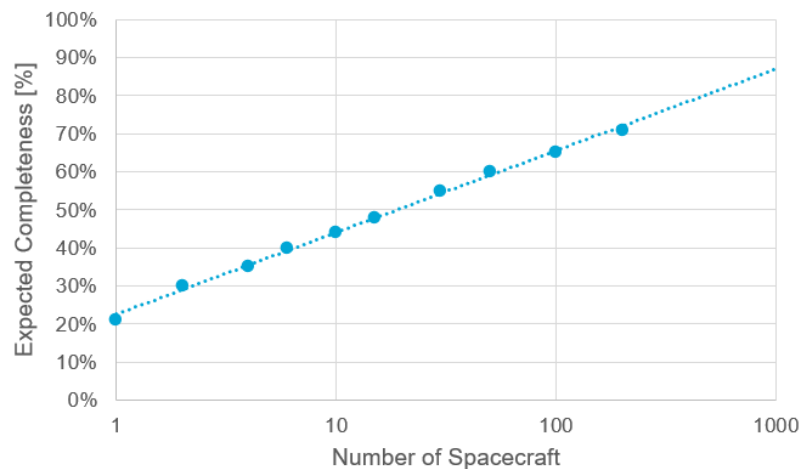


Figure 5.33: Expected performance as a function of number of spacecraft.

# 6

## Sensitivity Analysis

**6.1. Expected Performance**

**6.2. Optimization Results**

**6.3. Hardware and Survey Properties**



# 7

## Conclusion

### **7.1. Opportunities for Mission Design**

### **7.2. Recommendations for Further Research**



# A

## Verification and Validation

**A.1. Modelling of Observations**

**A.2. Survey-specific Properties**

**A.3. Survey Performance**

**A.4. Optimization**